# FEM ANALYSIS OF SURFACE ACOUSTIC WAVE RESONATORS OF PIEZOELECTRIC GALIUM NITRIDE ON SILICON SUBSTRATE FOR FREQUENCIES ABOVE 5 GHz

MASTER THESIS

UNIVERSITY OF CRETE
MICROELECTRONICS RESEARCH GROUP
GREECE

In collaboration with

IMT – BUCHAREST - ROMANIA

ATHANASIOS MARGIOLAKIS

2012

# ABSTRACT

The need for faster transfer rates in telecommunications are translated to the need for devices that share data in higher frequencies. This work is focused on investigating the properties of such a device, that is a surface acoustic wave resonator build by a Silicon substrate, a Gallium Nitride piezoelectric layer and Gold Interdigital Transducer (IDT) electrodes. A finite element model was designed and simulated in COMSOL Multiphysics environment to define the resonance frequencies. Parameters like IDT finger height/width, substrate height and different types of IDT structures were investigated on how they change the center resonant frequency and the admittance of the device. Simulations were done in a two dimensional space because a three dimensional simulation has very high computing requirements. These devices were fabricated in “FORTH” at Heraklion and characterized at “IMT” in Romania and the experimental results were compared with the simulated models.

# ACKNOWLEDGEMENTS

I would like to thank my supervisor Dr. George Konstantinidis for offering me the opportunity to work in the Microelectronics Research Group of the University of Crete, for supporting my work and providing assistance whenever I needed.

I would also like to thank the members of the IMT-Bucharest that I collaborated with, Dr. Dan Neculoiu for the guidance and education he provided me, Dr. Mircea Dragoman for the interesting conversations on microelectronics and not only, that we had. I want to thank Dr. Alexandra Stefanescu for the training on the simulation and the overall constant support she provided all this time, as also Dr. Adrian Dinescu for introducing me to the microelectronic fabrication techniques.

Lastly I would like to thank Dr. Eleftherios Iliopoulos who accepted me as his postgraduate student under his supervision and supported my work, and Dr. Alexandros Pantazis for his guidance on my primary work.

# Table of Contents

# INTRODUCTION

SAWs were first explained in 1885 by Lord Rayleigh, who described the surface acoustic mode of propagation and predicted its properties in his classic paper. Named after their discoverer, Rayleigh waves have a longitudinal and a vertical shear component that can couple with any media in contact with the surface. This coupling strongly affects the amplitude and velocity of the wave, allowing SAW sensors to directly sense mass and mechanical properties.

This kind of wave is commonly used in devices called SAW devices in electronic circuits. SAW devices are used as filters, oscillators and transformers, devices that are based on the transduction of acoustic waves. The transduction from electric energy to mechanical energy (in the form of SAWs) is accomplished by the use of piezoelectric materials.

Electronic devices employing SAWs normally use one or more interdigital transducers (IDTs) to convert acoustic waves to electrical signals and vice versa by exploiting the piezoelectric effect of certain materials (quartz, lithium niobate, lithium tantalate, lanthanum gallium silicate, etc.). These devices are fabricated by photolithography, the process used in the manufacture of silicon integrated circuits.

SAW filters are now used in mobile telephones, and provide significant advantages in performance, cost, and size over other filter technologies such as quartz crystals (based on bulk waves), LC filters, and waveguide filters.

Much research has been done in the last 20 years in the area of surface acoustic wave sensors. Sensor applications include all areas of sensing (such as chemical, optical, thermal, pressure, acceleration, torque and biological). SAW sensors have seen relatively modest commercial success to date, but are commonly commercially available for some applications such as touchscreen displays.

SAW resonators are often used in radio transmitters where tunability is not required. They are often used in applications such as garage door opener remote controls, short range radio frequency links for computer peripherals, and other devices where channelization is not required. Where a radio link might use several channels, quartz crystal oscillators are more commonly used to drive a phase locked loop. Since the resonant frequency of a SAW device is set by the mechanical properties of the crystal, it does not drift as much as a simple LC oscillator, where conditions such as capacitor performance and battery voltage will vary substantially with temperature and age.

SAW filters are also often used in radio receivers, as they can have accurately determined and narrow passbands. This is helpful in applications where a single antenna must be shared between a transmitter and a receiver operating at closely spaced frequencies. SAW filters are also frequently used in television receivers, for extracting subcarriers from the signal; until the analog switchoff, the extraction of digital audio subcarriers from the intermediate frequency strip of a television receiver or video recorder was one of the main markets for SAW filters. They are also often used in digital receivers, and are well suited to superhet applications. This is because the intermediate frequency signal is always at a fixed frequency after the local oscillator has been mixed with the received signal, and so a filter with a fixed frequency and high Q provides excellent removal of unwanted or interference signals.

# SURFACE ACOUSTIC WAVES THEORY

## 2.1. EXITATION REQUIREMENTS

Electronic signal processing by means of the selective manipulation of surface acoustic waves on piezoelectric substrates was initiated in 1965 with the invention of the thin-film interdigital transducer (IDT) by White and Voltmer at the University of California, at Berkeley. Their technique was to fabricate metal thin film IDTs on the surface of a suitable piezoelectric substrate that would act as electrical input transducer launched and manipulated a surface acoustic wave and converted it back to a suitably field electrical one. This surface acoustic wave type was a Rayleigh wave, with motion confined to within about one acoustic wavelength under the free surface of the piezoelectric.
Surface Acoustic Waves (SAW) are ultrasonic waves propagating along the surface of solids.
Surface acoustic waves can be generated at the free surface of an elastic solid. In the SAW devices considered in this text, the generation of such waves is achieved by application of a voltage to a metal-film IDT deposited on the surface of a piezoelectric solid. Two IDTs are required in the basic SAW device configuration sketched in Fig. 2.1. One of these acts as the device input and converts signal voltage variations into mechanical acoustic waves. The other IDTs is employed as an output receiver to convert mechanical SAW vibrations back into output voltages. Such energy conversions require the IDTs to be used in conjunction with elastic surfaces that are also piezoelectric ones. However, the surface outside the IDT regions need only be elastic, without being piezoelectric.
In that reciprocity applies to both systems, input and output IDTs may be likened to electromagnetic transmitting and receiving antennas. In principle, therefore, signal voltages can be applied to either IDT to give the same result. The aim of this is to create some advantageous signal-processing function through the interaction of acoustic waves, rather than through electromagnetic ones, while enjoying the compact device dimensions attainable with such processing.

## 2.2. MECHANICAL MOTION OF SURFACE ACOUSTIC WAVES

Let us consider the propagation of a Rayleigh wave on an unbounded elastic surface. As pictured in Fig 2.2, the physical motion of this SAW wave is mechanically with time-dependent elliptical displacement of the surface structure. One component of this physical displacement is normal to the surface. Distance $x$ relates to the SAW propagation axis, while $y$ is a surface normal axis in a Cartesian

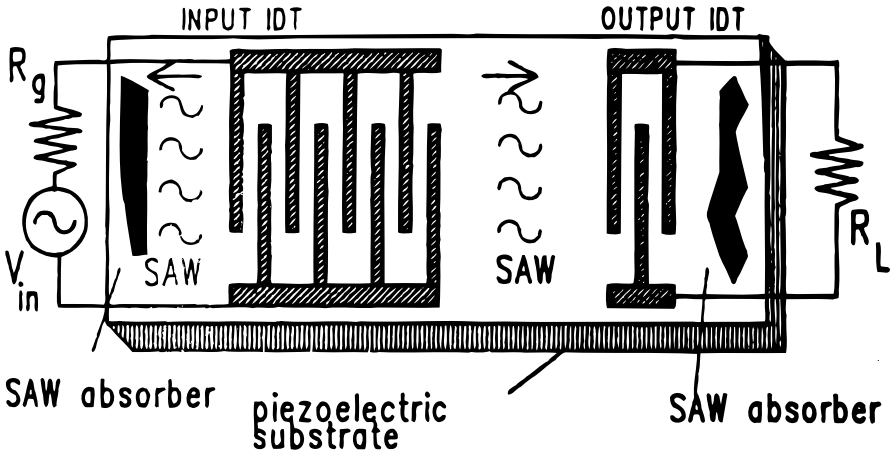


FIG 2.1. Basic unapodized SAW/pseudo-SAW delay line on piezoelectric substrate, with metal thin-film input/output interdigital transducers. The absorbers that are sometimes used to absorb spurious SAW transmissions resulting from IDT bidirectionality.[15]

coordinate system. Surface particle motion is predominantly in the *y*-*x*-plane in Fig. 2.2. The two wave motions are 90º out of phase with one another in the time domain, so that when one displacement component is maximum at a given instant the other will be zero. The amplitude of the surface displacement along the *y*-axis is larger than along the SAW propagation axis *x*. It is "easier" for the crystal structure to vibrate in the unbounded direction than in the bounded on. The amplitudes of both of these SAW displacement components become negligible for penetration depths greater than a few acoustic wavelengths $\lambda(=v/f)$ into the body of the solid. This phenomenon may be considered to be analogous to that of *skin depth*, relating electromagnetic wave penetration into a conductor.

## 2.3. STRESS AND STRAIN IN A NONPIEZOELECTRIC ELASTIC SOLID

Consider the relations between mechanical stress *T* and strain *S* for small static deformations of a nonpiezoelectric elastic solid. Stress is just the force *F* applied per unit area *A* of the solid. Stress, force and area can all be represented as vector quantities so that $\boldsymbol{T=F/A}$. The units of *T* are $N/m^2$ when force *F* is expressed in newtons (N). Strain *S*, which represents the fractional deformation due to force *F*, can be defined as $\boldsymbol{S=\Delta L/L}$(dimensionless), where $\Delta L$ is the fractional deformation of the solid of length *L*.

Stress and strains exerted within an elastic solid can exist in compressional or shear form. With compressional stress, for example, the applied force *F* is normal to the surface area *A* in Fig. 2.3. In either case they can be related proportionally

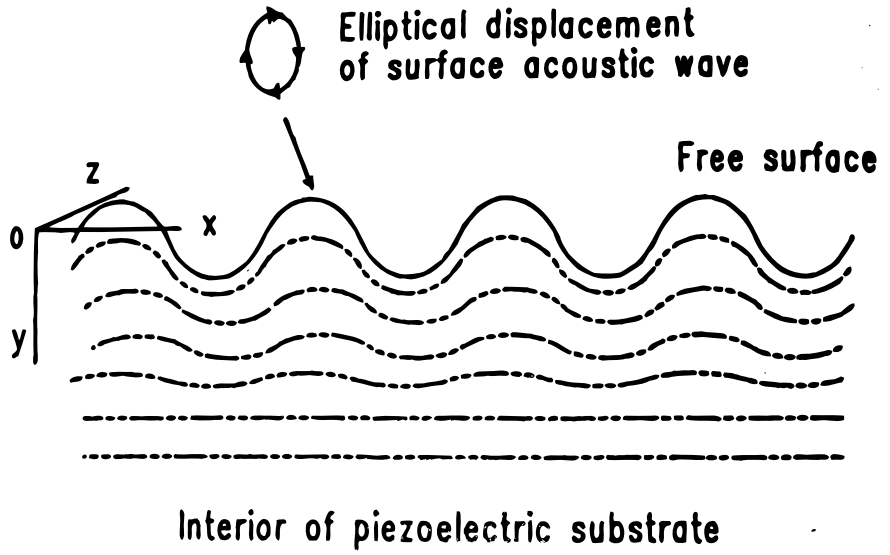


FIG 2.2. Non realistic representation of Rayleigh-wave motion on the surface of a piezoelectric substrate. While the illustration refers to a piezoelectric substrate, this is not a requirement for propagation but only for the excitation region.[15]

by Hooke's Law for elastic deformation. For simple compressional stress and strain along the same axis, this can be written as

$$T=cS \tag{2.1}$$

where $c$ = elastic stiffness coefficient, also known as Young's modulus ($N/m^2$). In general the above equation must be formulated to accommodate all possible components of stress and deformation so that

$$(T) = (c):(S), \quad T_{jk} = c_{jklm}\, S_{lm} \tag{2.2}$$

expressed as a *tensor equation* – with tensor terms identified by symbols ($_{xyz}$). For example, an expansion of tensor $(T)$ for values of $T_{xx}$ along the $x$-axis gives terms

$$\begin{aligned} T_{xx} = {} & c_{xxxx}S_{xx} + c_{xxxy}S_{xy} + c_{xxxz}S_{xz} \\ & + c_{xxyx}S_{yx} + c_{xxyy}S_{yy} + c_{xxyz}S_{yz} \\ & + c_{xxzx}S_{zx} + c_{xxzy}S_{zy} + c_{xxzz}S_{zz} \end{aligned} \tag{2.3}$$

Because force and area vectors need not be aligned, the stress parameter $T$ can be written as $T_{jk} = F_j/A_k$, where the first subscript $j$ denotes the direction of the force $F$ while the second subscript $k$ is the direction of the vector representing area $A$ in Fig. 2.3. Likewise, tensor strain terms can be given as $S_{lm} = \Delta_l/L_m$ for deformation directions defined by the second two suffixes. Here, (c) is referred to as

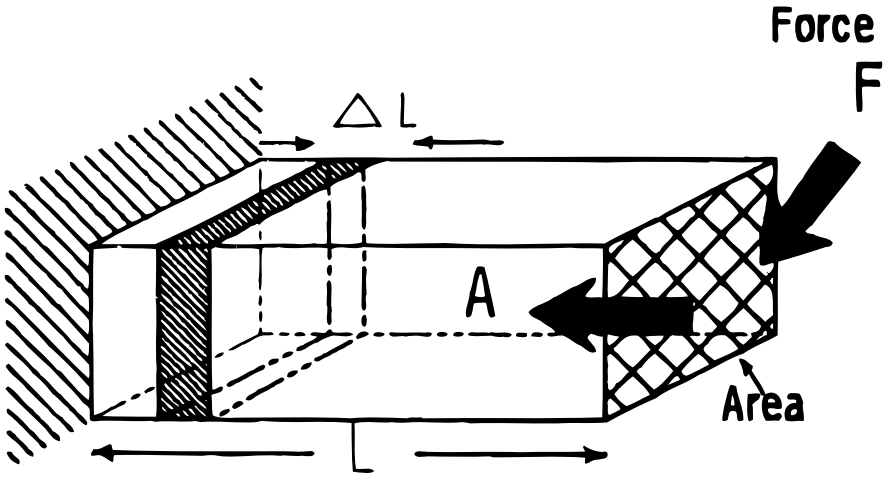


FIG 2.3. Notation used here for parameters relating to the deformation of an elastic solid. Note that *F* and *A* parameters can be vector quantities.[15]

a *fourth-rank tensor,* as its components have four suffixes $c_{jklm}$. Similarly, *(T)* and *(S)* are classed as *second-rank tensors*. Where *j=k=l=m* is specified along one axis (say, the *x*-axis, for example), $T_{xx} = c_{xxxx}S_{xx}$ relates compressional stress and strain along that axis. Tensor equation (2.2) can be reduced to a *matrix* equation [*T*] = [*c* ][*S* ] (denoted by symbols [x]), by redimentioning [*T*] and [*S*] so that they each have only one suffix instead of two as in Eq. (2.3). To this end, tensor components of *T* and *S* can be reduced to matrix components given by

$$T_1 = T_{11},\ T_2 = T_{22},\ T_3 = T_{33}$$
$$T_4 = T_{32} = T_{23},\ T_5 = T_{31} = T_{13},\ T_6 = T_{12} = T_{21} \tag{2.4}$$

$$S_1 = S_{11},\ S_2 = S_{22},\ S_3 = S_{33}$$
$$S_4 = S_{32} = S_{23},\ S_5 = S_{31} = S_{13},\ S_6 = S_{12} = S_{21} \tag{2.5}$$

In this way, the elastic stiffness constant is reduced to a 6 × 6 matrix [*c*], with 36 possible independent values relating the six (reduced) components of stress to the six (reduced) components of strain. Moreover, from energy and symmetry considerations, these 36 possible independent terms can be reduced to a maximum of 21 for the most general crystal symmetry examples. A further reduction is made possible by an appropriate choice of reference coordinate axes in relation to crystal axes. For example, cubic crystals with coordinate reference axes *x*, *y*, *z*, chosen parallel to crystal axes *X*, *Y*, and *Z* have their number of independent elastic constant coefficient terms in [*c*] reduced from 31 to just 3, as shown in Eq. (2.6).

$$CUBIC\begin{pmatrix}T_1\\T_2\\T_3\\T_4\\T_5\\T_6\end{pmatrix}=\begin{pmatrix}c_{11}&c_{12}&c_{12}&0&0&0\\c_{12}&c_{11}&c_{12}&0&0&0\\c_{12}&c_{12}&c_{11}&0&0&0\\0&0&0&c_{44}&0&0\\0&0&0&0&c_{44}&0\\0&0&0&0&0&c_{44}\end{pmatrix}\begin{pmatrix}S_1\\S_2\\S_3\\S_4\\S_5\\S_6\end{pmatrix} \tag{2.6}$$

Silicon (Si), which is not piezoelectric, falls into this class of cubically symmetric crystals.

On the other hand, the number of independent coefficients in the elastic constant matrix [$c$ ] reduces to five when the $z$-reference coordinate is chosen along the Z-axis of a hexagonal crystal

## 2.4. PIEZOELECTRIC INTERACTIONS

The electric field $E$ established by applied voltage $V$ will cause distortion of the otherwise neutral molecular charge distributions in the insulator, in turn this will result in an accumulation of surface charge on the capacitor plates. The surface charge of *density D* ($C/m^2$) will be proportionally related to $E$ by

$$D = \varepsilon_r\varepsilon_0 E = \varepsilon E\ , \tag{2.7}$$

where $\varepsilon_r$ = relative dielectric permittivity, or dielectric constant (dimensionless), and $\varepsilon_0$ = permittivity of free space = $8.856 \times 10^{-12}$ F/m.

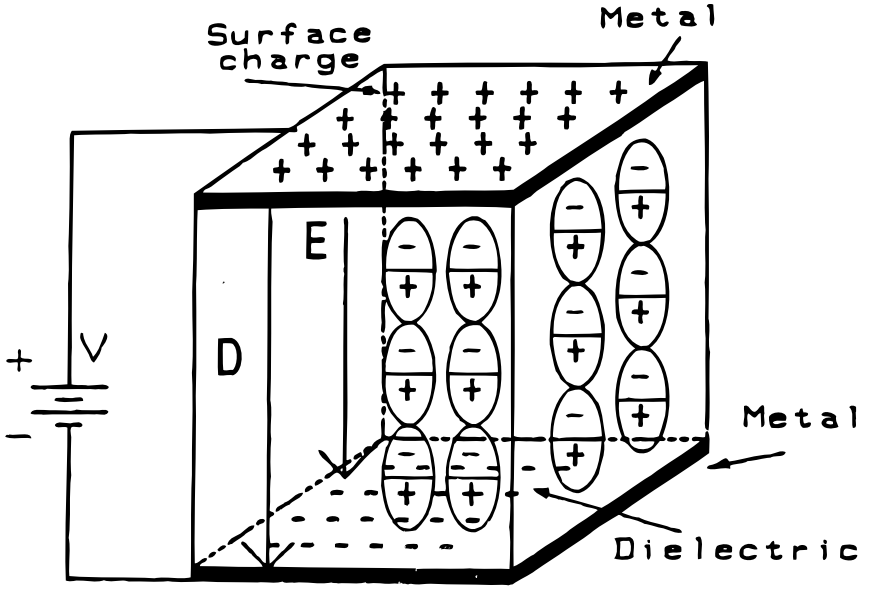


FIG 2.4. Displacement density $D$ and electric-field intensity $E$ vectors in simple plane-parallel capacitor containing a solid nonpiezoelectric dielectric.[15]

The simple relation of Eq. (2.7) no longer holds for piezoelectric dielectrics. Because of coupling between electrical and mechanical parameters, the application of an electric field stimulus will give rise to mechanical deformations and vice versa. Mathematically, this interaction can be expressed in terms of a piezoelectric constant matrix [e] (with units of $C/m^2$) such that the electrical displacement density $D$ is given by a matrix equation

$$D = [e\,][S] + [\varepsilon\,]E\,, \tag{2.8}$$

where $S$ = strain and $E$ = electric field intensity as before. Here, permittivity $\varepsilon$ is as measured at zero or constant strain. Equation (2.8) is a matrix equation employing the reduced coordinates for strain $S$ in Eq. (2.5). The displacement density term is a three-dimensional one in $x$, $y$ and $z$ coordinates. Because the $S$ term has six components from Eq. (2.5), the piezoelectric constant terms in [$e$] will form a 3 × 6 matrix with 18 elements. The parameter [$\varepsilon$] relating dielectric permittivity is a 3 × 3 matrix with 9 elements.
In addition, for piezoelectric materials the mechanical stress relationships are extended to

$$[T] = [c][S] - [e^t]E\,, \tag{2.9}$$

where $[e^t]$ is now a 3 × 6 matrix and is the transpose of the piezoelectric constant [$c$] (i.e., matrix rows and columns are interchanged). Equations (2.8) and (2.9) are often referred to as constitutive equation.
The element values of [$e$] will depend on the symmetry properties of the piezoelectrics with trigonal crystal classification, these are

gallium nitride (cubic class)

$$[e] = \begin{pmatrix} 0 & 0 & 0 & 0 & e_{15} & 0 \\ 0 & 0 & 0 & e_{15} & 0 & 0 \\ e_{31} & e_{31} & e_{33} & 0 & 0 & 0 \end{pmatrix} \tag{2.10}$$

For SAW wave propagation in piezoelectrics, it may be shown that the electromechanical coupling coefficient $K^2$ can be defined in terms of the piezoelectric coefficient $e$, elastic constant $c$ and dielectric permittivity $\varepsilon$ already considered herein, where

$$K^2 = \frac{e^2}{c\varepsilon} \tag{2.11}$$

and tensor subscripts have been dropped in Eq. (2.11). Appropriate constants depend on both the crystal cut and the propagation direction of the surface acoustic wave. Additionally, the parameter $K^2$ in Eq. (2.11) can be derived experimentally.

## 2.5. GENERAL EQUATIONS FOR SURFACE WAVES AND BULK WAVES

The propagation of acoustic waves in an anisotropic piezoelectric crystal may be described in terms of a set of six linear equations. These are:

**Equations of motion:**
$$\frac{\partial T_{ij}}{\partial x_i} = \rho \frac{\partial^2 u_{\mathrm{j}}}{\partial \mathrm{t}^2} \tag{2.12a}$$

**From Maxwell's equations, (quasi-static):**
$$\frac{\partial D_i}{\partial x_i} = 0 \tag{2.12b}$$

**Electric field intensity:**
$$E_i = -\frac{\partial \Phi}{\partial x_i} \tag{2.12c}$$

**Piezoelectric mechanical stress from Eq. (2.9):**
$$T_{ij} = c_{ijkl} S_{kl} - e_{nij} E_n \tag{2.12d}$$

**Piezoelectric displacement density from Eq. (2.8):**
$$D_m = e_{mkl} S_{kl} + \varepsilon_{mn} E_n \tag{2.12e}$$

**Linear strain displacement:**
$$S_{kl} = \frac{1}{2}\frac{\partial u_k}{\partial x_l} + \frac{\partial u_l}{\partial x_k} \tag{2.12f}$$

where *S*=strain, *T*=stress, *ρ*=mass density, *u*=mechanical displacement, *D*=displacement density, *E*=electric field intensity, and *Φ*=electric potential.
Three of these variable indices relate to the three Cartesian coordinates for displacement *u*, while the fourth index applies to potential Φ. The total solutions for *u* and Φ are taken to be linear combinations of the ensuring partial-wave equations applied to the piezoelectric. For the *x, y, z* spatial coordinate the travelling wave displacement and potential in the piezoelectric interior at reference time *t*=0 are given by

$$\mathrm{U_i} = \sum_{n=1}^{4} u_{\mathrm{i}}^{(\mathrm{n})} e^{j(\omega t - \beta x)}\, e^{-\alpha_n |y|} \qquad (i = 1\ to\ 3) \tag{2.13a}$$

$$\Phi = \sum_{n=1}^{4} \Phi_4^{(\mathrm{n})} e^{j(\omega t - \beta x)}\, e^{-\alpha_n |y|} \tag{2.13b}$$

where the (*n*) superscripts refer to the solution corresponding to the chosen root $\alpha_n$, while $u_{\mathrm{i}}^{(n)}$ (for *i*=1 to 3, *n*=1to 4) are the mechanical amplitude coefficients, $\Phi_4^{(\mathrm{n})}$ (for *n*=1 to 4) are potential amplitude coefficients, and $\beta = \omega/v = 2\pi f/v$=phase constant, where *v*=wave velocity. Moreover, the root parameters $\alpha_n$ themselves are actually *propagation constants* (also known as decay constants), with units of metre$^{-1}$. As such, they may have a) pure real, b) pure imaginary or c) complex values as functions of frequency.
In describing surface wave and bulk wave propagation, it is often convenient to relate these as a function of inverse phase velocity $1/v_p$ (or *slowness*), rather than directly as a

direct function of the phase velocity $v_p$ parallel to the substrate surface. Moreover, the use of an *effective surface permittivity* $\varepsilon_s$ parameter (which is usually plotted as a function of slowness *s*), represents another useful analytical tool. This effective surface permittivity has been derived in the form

$$\varepsilon_s = \frac{\sigma}{\beta\Phi} \qquad (at\ y = 0), \tag{2.14}$$

where $\sigma$=surface change density (coulomb/metre$^2$), $\beta$=phase constant, and $\Phi$=surface potential (volts). Effective permittivity $\varepsilon_s$=$\infty$ for a metalized surface with zero potential $\Phi$. The effective permittivity can be complex, so that $\varepsilon_s = \varepsilon'_s - j\varepsilon''_s$.

S-Parameters

Reflection and transfer function of devices are well suited to be represented by S-Parameters. Thus, S-parameters can define the complete small signal characteristics of a device excluding noise. Similar to the signal flow definitions and the reflection coefficient, the S-parameters are based on the relationship between the incoming and outgoing waves.

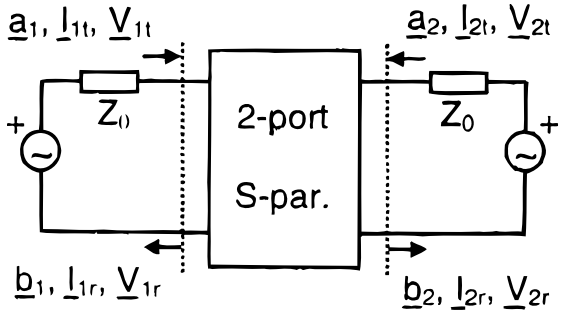


FIG 2.5 Source and load transmission and reflection power wave parameters of a 2-port.[14]

As shown in Fig. 2.5 for a typical 2-port, S-parameters are based on the wave parameters $\underline{a}_j$ and $\underline{b}_k$, which determine the transmitted and reflective parameters, respectively, of the signal at or between a node. The power wave parameters are a function of the transmitted and reflected voltages $\underline{V}_t$ and $\underline{V}_r$ , and are defined by

$$\underline{a}_j = \frac{\underline{V}_{jt}}{\sqrt{Z_0}}$$

$$\underline{b}_k = \frac{\underline{V}_{kr}}{\sqrt{Z_0}}$$

Analogously, the last two equations could also be determined be the transmitted and reflected currents. The products $\underline{a}_j\underline{a}_j^*$ and $\underline{b}_k\underline{b}_k^*$ are proportional to the responding real powers. Per definition, only one reference source is active calculation of a specific S-parameter, while all others are set to zero. Note the signal of the transfer function is directed from node j to node k. The parameter set of a network consists of all possible relations between the wave parameters excluding the relationship between the same parameters of the number of power wave parameters and S-parameters amounts to $2^n$ denotes the number of ports.

| **Input reflection coefficient** | **Output reflection coefficient** |
|---|---|
| $\underline{S}_{11}=\frac{\underline{b}_1}{\underline{a}_1}\ \|\underline{a}_2=0$<br>Ratio of reflected power to incoming power at port 1<br>No power fed from port 2<br>Port 2 terminated with $Z_0$ | $\underline{S}_{22}=\frac{\underline{b}_2}{\underline{a}_2}\ \|\underline{a}_1=0$<br>Ratio of reflected power to incoming power at port 2<br>No power fed from port 1<br>Port 1 terminated with $Z_0$ |
| **Forward transmission coefficient** | **Reverse transmission coefficient** |
| $\underline{S}_{21}=\frac{\underline{b}_2}{\underline{a}_1}\ \|\underline{a}_2=0$<br>Ratio of outgoing power at port 2 to incoming power at port 1<br>No power fed from port 2<br>Port 2 terminated with $Z_0$ | $\underline{S}_{12}=\frac{\underline{b}_1}{\underline{a}_2}\ \|\underline{a}_1=0$<br>Ratio of outgoing power at port 1 to incoming power at port 2<br>No power fed from port 1<br>Port 1 terminated with $Z_0$ |

***Table 2.1.*** *Definition of 2-port S-parameters*

In many cases, 2-ports are applied, e.g. also for transistors, where the third port serves as the common ground. A 2-port can be fully described by the set of 4 S-parameters, namely the input reflection, output reflection, forward transmission and reverse transmission coefficient. The corresponding S-parameter definitions are summarized in Table 2.1. These parameters can be found in typical transistor data sheets and depend on the frequency and the applied DC bias.

The reflection coefficient $\underline{\Gamma}_{11}$ and $\underline{S}_{11}$ are very similar. The only difference is that as per definition $\underline{S}_{11}$ is terminated with $Z_0$ at port 2, whereas $\underline{\Gamma}_{11}$ considers any termination at port 2. Given that $\underline{Z}_2=Z_0$, which is the case in typical measurement environments we obtain $\Gamma_{11}=S_{11}$

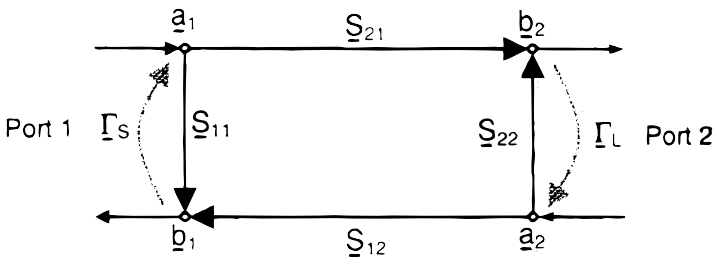


FIG 2.6 Calculation of $\underline{\Gamma}_{11}=\frac{\underline{b}_1}{\underline{a}_1}$ of a device characterized by its S-parameters and terminated by an output load with $\underline{\Gamma}_L$ using Mason's rule.[15]

Let us prove the later claim by applying the Mason's rule. As an exercise, we calculate $\underline{\Gamma}_{11}$. Referring to Fig.2.6, the input characteristics of a device are determined by its S-parameter and the load impedance represented by $\underline{\Gamma}_L$. Please note that $\underline{\Gamma}_S$ is not considered since there is no source termination when evaluating $\underline{\Gamma}11$. Directed from $\underline{a}1$ to $\underline{b}1$ , there are forward paths $\underline{P}_1=\underline{S}_{11}$ and $P_2=S_{21}\Gamma_L S1_2$. We can identify $S_{22}\Gamma_L$ as the only loop yielding $\Delta=1-S_{22}\Gamma_L$. Now we can calculate the input reflection coefficient by means of the below equation:

Eq. $\underline{\Gamma}_{11}=\frac{\underline{b}_1}{\underline{a}_1}=$

On the condition that $\underline{Z}_2=Z_0$ we obtain $\underline{\Gamma}_L=0$ and consequently $\underline{\Gamma}_{11}=\underline{S}_{11}$ as we have to prove. Analogously, we can determine the output characteristics with respect to the input termination $\underline{\Gamma}_S$. For $\underline{\Gamma}_{22}$ we can deduce

Eq. $\frac{\underline{b}_1}{\underline{a}_1}$

Given that $\underline{Z}_S=Z_0$ we obtain $\underline{\Gamma}_{22}=\underline{S}_{22}$ as expected

## Static Capacitance

The term “electrostatic” means that the effect of wave excitation and/or propagation is ignored and/or negligible.[5]
When the IDT is infinitely long and all the electrode widths and spaces are equal, the static charge distribution $q(x_1)$ can be given in analytical form. The charge distribution $q(x_1)$ for the single-electrode-type IDT is given by

$$q(x_1) = V\frac{C_s}{\sqrt{\cos(4\pi x_1/p_I) - \cos(2\pi\omega/p_I)}} \times \frac{2\sqrt{2}}{p_I \cdot P_{-1/2}\{\cos(2\pi\omega/p_I)\}} \tag{2.15}$$

and that on the split-electrode-type IDT is given by

$$q(x_1) = V\frac{C_s \cos(2\pi x_1/p_I)}{\sqrt{-\cos(8\pi x_1/p_I) - \cos(4\pi\omega/p_I)}} \times \frac{2\sqrt{2}}{p_I \cdot P_{-1/4}\{\cos(4\pi\omega/p_I)\}} \tag{2.16}$$

where $C_S$ is the static capacitance for the IDT per period given by

$$C_S = \mathrm{W}\epsilon(\infty)\frac{P_{-1/2}\{\cos(2\pi\omega/p_I)\}}{2P_{-1/2}\{-\cos(2\pi\omega/p_I)\}} \tag{2.17}$$

for the single-electrode-type IDT and

$$C_S = \mathrm{W}\sqrt{2}\epsilon(\infty)\frac{P_{-1/4}\{\cos(4\pi\omega/p_I)\}}{2P_{-1/4}\{-\cos(4\pi\omega/p_I)\}} \tag{2.18}$$

for the split-electrode-type IDT, respectively. W is the aperture of the IDT, ω is the electrode width, $P_u(x)$ is the Legendre function, and $\epsilon(S)$ is the effective permittivity. Under the low-frequency approximation, $\epsilon(\infty)$ is given by

$$\epsilon(\infty) = \epsilon_0 + \sqrt{\epsilon_{11}^T \epsilon_{33}^T - \epsilon_{13}^{T2}} \tag{2.19}$$

where $\epsilon^T$ is the permittivity measured under the no stress condition, which is different from that measured under the zero strain condition.

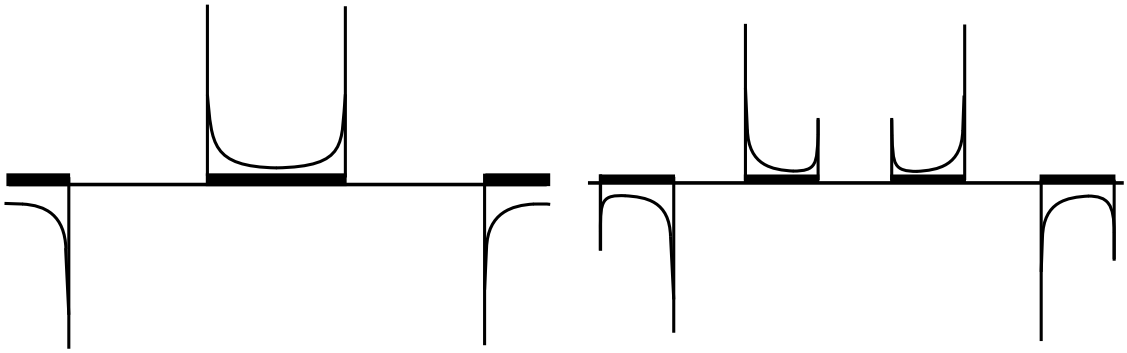

FIG 2.7 Charge distribution in a single and Split-electrode IDT array.[14]

Figure 2.7 shows $q(x_1)$ calculated by (2.15) and (2.16). The charge concentrates at the electrode edges and diverges as $1/\sqrt{x}$. This fact makes the calculation of charge distribution on the IDT complex.[9]

# FILTER DESIGN

## 3.1. IDEAL LINEAR-PHASE RESPONSE

Consider the overall transfer function $H(f)$ of a SAW filter employing bidirectional IDTs, as sketched in Fig. 3.1. This can be evaluated with reference to the block diagram of Fig. 3.2, which shows that $H(f)$ comprises thee component terms. Two of these relate the individual responses $H_1(f)$ and $H_2(f)$ of input and output IDTs, respectively, while the third term is associated with the transmission path between the IDTs. The overall transfer function is:

$$H(f) = \frac{V_{out}}{V_{in}} = H_1(f)H_2^*(f)e^{-j\beta x(f)} \tag{3.1}$$

where $|H(f)| = |H_2^*(f)|$ here the conjugate response $H_2^*(f)$. In Eq. (3.1) the phase delay term between input and output IDTs is given as $e^{-j\beta x(f)}$ where $\beta = 2\pi/\lambda = 2\pi f/v$ is the phase constant, an $x(f)$d is a frequency-dependent separation between those segments of input and output IDTs that are excited at signal frequency $f$ [10]. This relates to the general case where IDTs can have arbitrary finger separation. For the specific example of Fig. 3.3, where input and output IDTs have uniform finger apodization overlap, $x(f)$ reduces to $x(f) = d$, where $d$ is the distance between the midpoints of the bidirectional input and output IDTs.

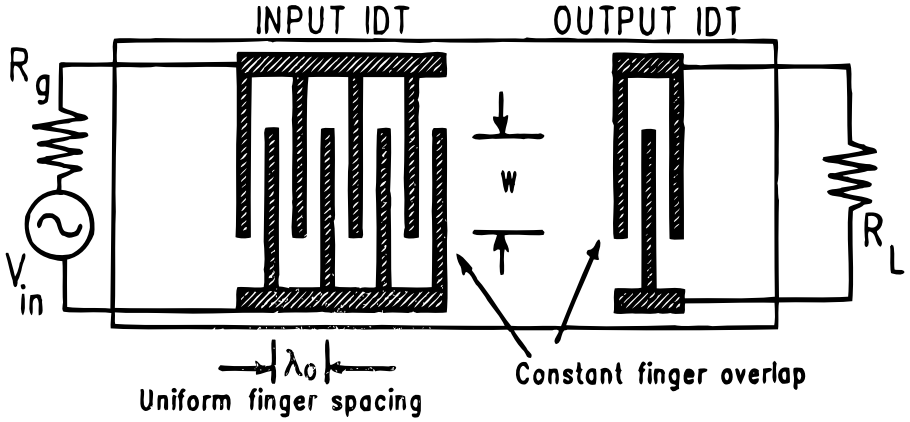


FIG 3.1. Elementary structure comprising input and output IDTs with uniform finger spacing and constant overlap (apodization).[15]

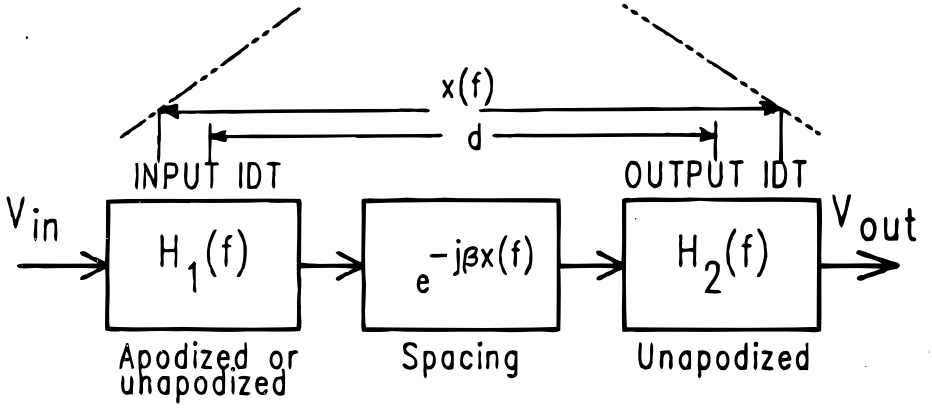


FIG 3.2. Elementary structure comprising input and output IDTs with uniform finger spacing and constant overlap (apodization).[15]

This signifies as if all the SAW emissions from the excited input IDT emanate from a common midsection, while those arriving at the output IDT are summing at that midsection. Moreover, at this axis the relative phase shifts of individual response functions $H_1(f)$ and $H_2(f)$ simply become 0º or 180º, depending on which way the electrical leads are attached. As a result, the phase shift of this type of SAW filter is due entirely to the separation between IDT midsections, and given by $e^{-j\beta d}$[14]. This will give linear-phase response because phase angle $<\beta d$ varies linearly with frequency. The desired amount of filter time delay, or phase shift at a given frequency, is then simply achieved by selecting the spacing between IDTs. This type of SAW filter is usually known as a SAW *delay line*.

This linear relationship holds for the IDTs of Fig. 3.3, where the overlap of adjacent electrode fingers is constant (i.e., uniformly apodized). As will be demonstrated in what follows, it also holds true when either or both IDTs are apodized, provided that the apodization pattern is symmetric about the IDT central axis.

## 3.2. DEVIATIONS DUE TO SECOND-ORDER EFFECTS

As with all other filters, however, practical SAW filters are not ideal devices. Various second-order affects will perturb the ideal environment to some degree, and degrade the filter response. The principal second-order effects that corrupt SAW filter responses are ahead.

1. Electromagnetic feed through, which relates to the direct coupling of input signal from input to output IDTs, in the form of electromagnetic radiation. Essentially, the two IDTs act as capacitor plates, which may be separated by only few acoustic wavelengths. The amount of electromagnetic feed through, which increases with frequency as the capacitive reactance decreases, can be significant. This feed through is coupled to the output

IDT at the velocity of light, to interact with the SAW signal arriving there. This interaction gives rise to periodic ripples of amplitude and phase across the SAW filter pass band at ripple frequency$f_r = 1/\tau$, where $\tau = d/v$ is the SAW propagation time between IDT phase centers separated by distance *d*. This can be one of the most troublesome sources of interference in SAW devices. (Others include parasitic due to packaging and bonding wires)

2. Triple-transit-interference is due to multiple SAW reflections between bidirectional input and output IDTs. This is normally associated with regenerative affects caused by current flow in the IDTs. Some of the SAW power received by the output IDT is reradiated into the piezoelectric. That portion from the output IDT that arrives back at the input can lead further regeneration of a SAW wave. As a result, the main voltage signal induced in the output IDT is corrupted by additional voltages due to these multiple SAW reflections. The path differences between the main and doubly reflected SAW signals result in amplitude and phase ripple across the SAW pass band, at a ripple frequency $f = 1/2\tau$.
3. The thin metal film IDT fingers deposited on the piezoelectric crystal surface introduce impedance and mass-loading discontinuities, so that a portion of the surface wave is reflected from both the front and back surface of each finger. This has two major effects. First, this will lead to a pronounced distortion of the radiation conductance of the IDT for film-thickness ratio $h/\lambda_0$>~1%, which can most beneficially be applied to the design of RF filters and resonator-filter structures, as well as some high-frequency IF filter designs (these will be neglected until introduced in Chapter 9). Further, multiple SAW reflections can occur between input and output IDTs to form an additional source of triple-transit interference.
4. Bulk-wave interference, which was already introduced in Chapter 2, will corrupt the pass band amplitude and phase response, as well as reduce the out-of-band amplitude rejection levels. It will also lead to increased filter insertion loss.
5. Circuit factor loading results from the finite source and load impedances that are external to the SAW filter. Both the input and output impedances of a SAW filter are frequency-dependent parameters. The consequence of this is that an input voltage will be divided between source resistance and filter input impedance in a frequency-dependent way unless compensation is made. The same situation applies to the output transducer circuitry.
6. In the input IDT circuitry, signal power is divided between the generator resistance and a fictitious resistance associated with SAW power radiation into the acoustic substrate medium. Maximum power transmission be the SAW wave occurs only when the two resistances are matched (i.e., equal). The same situation arises with the load changes result in insertion loss increases or changes due to mismatching.
7. Diffraction occurs in SAW IDTs in much the same way as it does in optical systems. Ideally, the SAW emissions induced by, and travelling under, excited IDT electrodes should have “flat” wavefronts, so that all parts of a wavefront launched by one IDT finger arrive at a receiving IDT finger after the same time delay. As in optics the SAW wave-

front will be spherical to a degree dependent on the aperture of the radiating source. This will corrupt the filter response. Anisotropy of the piezoelectric medium will also give rise to focusing or defocusing of the surface wave.

8. Excited IDT fingers can generate SAW waves at harmonic signal frequencies in addition to those generated at the fundamental signal frequency. (This may be desirable or undesirable feature, depending on the application) The levels of such harmonic frequencies will be dependent on the relative width of the metal fingers with respect to their separations. They will also depend on the overall IDT geometry used. This can lead to undesirable levels of harmonic response outside the passband of the fundamental signal. In some applications, however, the SAW filter is designed to operate at a desired harmonic frequency, while suppressing the fundamental at the same time.
9. Ground loops can be particularly troublesome in design of compact mobile and wireless communications circuitry. With reference to Fig. 3.3, many SAW filter designs have one pad of both the input and output IDTs “grounded”, for ease of fabrication. This can give rise to performance degradation, due to spurious coupling between circuit stages.

## 3.3. THE DELTA-FUNCTION MODEL

The *delta-function* model provides basic information on the transfer function response of a SAW filter. It can only treat some of the second-order effects considered in the preceding. It cannot provide information on filter input-output impedance levels, circuit factor loading, harmonic operation, bulk wave interference or diffraction. Because it cannot cater to impedances, the transfer function determination yields only relative insertion loss as a function of frequency. Despite these modeling limitations, it can still provide excellent preliminary design information on the response of a SAW filter using bidirectional IDTs in input and output stages, as absolute values of insertion loss are not predicted by this model.

The delta-function model approximates the complex electric-field distribution between adjacent fingers of an excited IDT, as a discrete number of delta-function sources. As illustrated in Chapter 2, the propagation of a surface wave on a piezoelectric may be associated with travelling waves of surface potential $\Phi$ and electric-field intensity $E$ produced and emanating from an exited IDT. While

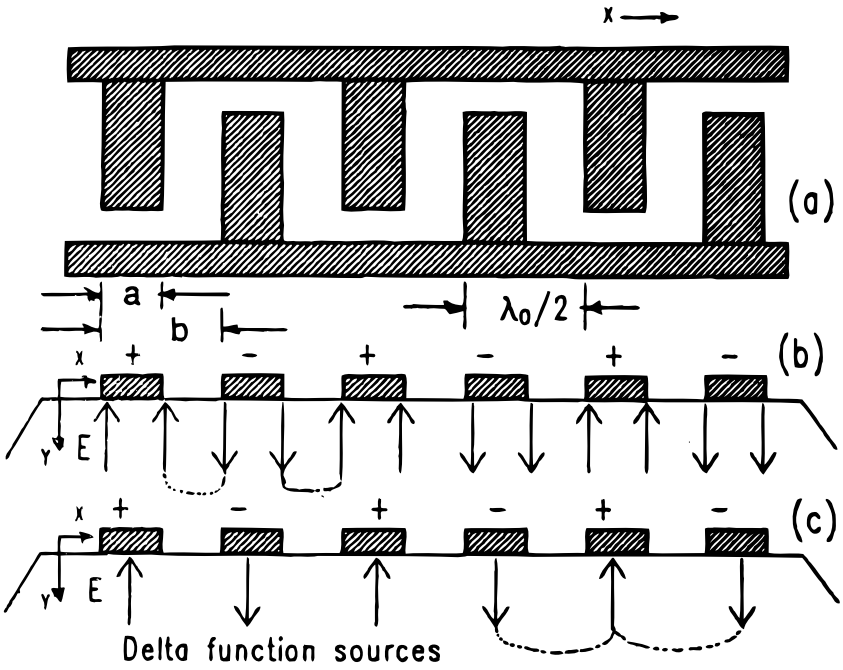


FIG 3.3. (a) Bidirectional IDT with uniform IDT. (b) Delta-function modeling of *E*-field distribution in xy-plane under excited IDT, with sources at finger edges. (c) Simpler delta-function model employs one source field under each electrode.[15]

the distribution of the time-varying electric field under adjacent electrodes is complex, it may be approximated as normal to the piezoelectric surface. It is designated as $E_{xy}$ in the *xy*-plane, in the sketch of Fig. 3.3(a).

Consider that Fig. 3.3(a) relates to the input IDT with response $H_1(f)$. As depicted in this figure, electrode fingers alternate in voltage polarity, with centers spaced $\lambda_0/2$ at center frequency $f_0 = v/\lambda_0$, so that SAW emissions under the IDT add constructively at this frequency. The metallization ratio $\eta$ relating a relative finger width and spacing is given by $\eta = a/b$. The intensity of the electric-field distribution will be proportional to the instantaneous change accumulation on adjacent electrode fingers due to input voltage $V_{in}$ established by the time-dependent input signal. At any instant, adjacent electrodes have opposite voltage polarity and opposite charge accumulation. Because unlike charges attract, these migrate to the edges of the IDT fingers. The resultant charge distribution can be modeled as delta-function sources of electric-field intensity $E_y$ at the finger edges. As depicted in

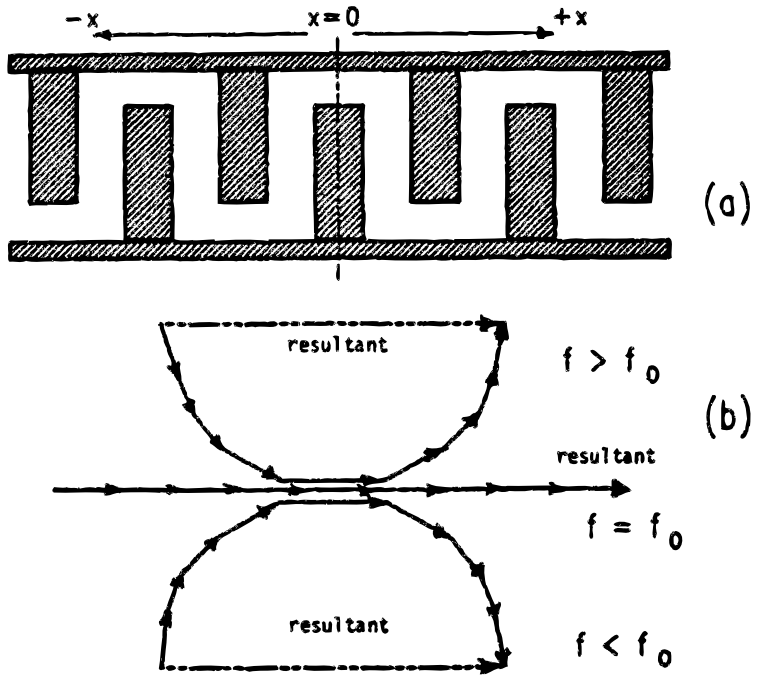


FIG 3.4. (a) Reference axis $x = 0$ at midpoint of uniform IDT. (b) When delta-function modeling is applied to excited IDT, the resultant relative phase angle of associated transfer function is always 0° or 180° at $x = 0$.[15]

Fig. 3.3(b), each electrode finger will have two delta sources of electric-field intensity associated with it, which amplitudes are proportional to the applied voltage. The directions and relative field polarities will alternate in pairs from finger to finger. A summation of these delta sources can be used to simulate the resultant electric field intensity of the excited IDT in either the input or output stages. The overall transfer response can be obtained when this summation process is extended to include both IDTs. While the delta-function model can be used as it stands, with two delta-function sources associated with each excited electrode, it can be further simplified for computational convenience. As the delta-function special significance in employing a metallization ratio can be employed for this computation, there is no need to associate two delta-function excitation sources with each electrode. Two delta functions at finger edges can be replaced by one equivalent delta-function source at the center of each finger, sketched in Fig. 3.3(c).

The spatially distributed delta-function contributions may be summed at a convenient reference point along the *x*-axis. Consider that this reference is taken as *x*=0 at the center of the IDT as shown in Fig. 3.4(a). Moreover, assume the IDT has an odd number *N* of electrodes, so that *x*=0 is at the center of an electrode. Because only relative insertion loss can be obtained from this model, the amplitudes of the delta-function sources at each electrode can be normalized to a value $|E_y|$=1. The summation of sources yields the frequency response $H_1(f)$.

Although the amplitudes of the delta sources are constant, their individual phase angles at the point of summation $x$=0, will depend on the distance $x$ from each source to this summation point. Individual phase-shift terms are $e^{-j\beta x_n}$ for electrodes located at discrete points $-x_N \leq x_N \leq +x_N$ over the length of the IDT. The resultant frequency response $H_1(\beta) = H_1(f)$ is

$$H_1(f) = \sum_{n=-(N-1)/2}^{(N-1)/2} (-1)^{\mathrm{n}} A_n \, e^{-j\beta x_n} \tag{3.2}$$

where the term $(-1)^{\mathrm{n}}$ relates the alternating electrode polarity, while $A_n$ is an amplitude parameter proportional to the finger apodization overlap. This may be normalized to $A_n$=1 for the uniformly apodized IDT.

Equation (3.2) may be reformulated by employing the trigonometric equivalent of the exponential term, so that

$$H_1(f) = \sum_{n=-(N-1)/2}^{(N-1)/2} (-1)^{\mathrm{n}} A_n \, [\cos(\beta x_n) - j\sin(\beta x_n)] \tag{3.3}$$

The significance of choosing the reference axis $x$=0 at the center of the IDT becomes apparent. From trigonometric identities $\cos(\theta)=\cos(-\theta)$ and $\sin(\theta)=-\sin(\theta)$, it is seen that the imaginary (i.e. $j$ sin) terms in Eq. (3.3) cancel out in pairs, so that the summation for $H_1(f)$ is entirely in terms of the purely real quantity $\cos(\beta x)$. When the reference axis is taken at the midpoint of the symmetric structure, the phasor relating $H_1(f)$ as a function of frequency will always lie along the real axis in the complex plane, as sketched in Fig. 3.4(b). Its relative phase at this point will always be just 0º or 180º, depending on which way the electrical leads are connected. To obtain the bandpass response of the IDT about some center frequency $f_0$, now express frequency $f$ in Eq. (3.3) as $f = \{(f - f_0) + f_0\}$. After some manipulation, an expansion of Eq. (3.3) with $A_n$=1, yields a cosine series given by:

$$\begin{aligned} H_1(f) = 1 + 2cos\left(\pi \frac{f - f_0}{f_0}\right) + 2cos\left(2\pi \frac{f - f_0}{f_0}\right) \\ + \ldots . + 2cos\left(N_p \pi \frac{f - f_0}{f_0}\right) \end{aligned} \tag{3.4}$$

where $N_p = (n-1)/2 \approx N/2$ for large odd $N$ and $N_p = N/2$ for even $N$, and represents the number of electrode finger pairs in the IDT. Close to the center frequency $f_0$, Eq. (3.4) approximates a sinc function response given by

$$|H(f)| \propto \left|\frac{sinX}{X}\right| \propto \left|\frac{sin\left[N_p\pi(f-f_0)/f_0\right]}{N_p\pi(f-f_0)/f_0}\right| \tag{3.5}$$

where the sinc function is defined as $sinc(X) = (sinX)/X$.

An inspection of Eq. (3.5) indicates that the first nulls of the response about $f_0$ occur when $sin\left[N_p\pi(f-f_0)/f_0\right] = \sin(\pi)$, or $N_p = f_0/(f-f_0) = 2/BW_{nn}$ where $BW_{nn}$ is the fractional bandwidth between first nulls on either side of $f_0$. It may be shown that $BW_{nn} \approx 2.BW_4$, where $BW_4$ is the fractional bandwidth to the 4-dB amplitude points about the main response lobe. Expressed as a percentage, $BW_4\% \approx (100/N_p)\%$ where $N_p$ is the number of the electrode pairs in the IDT.

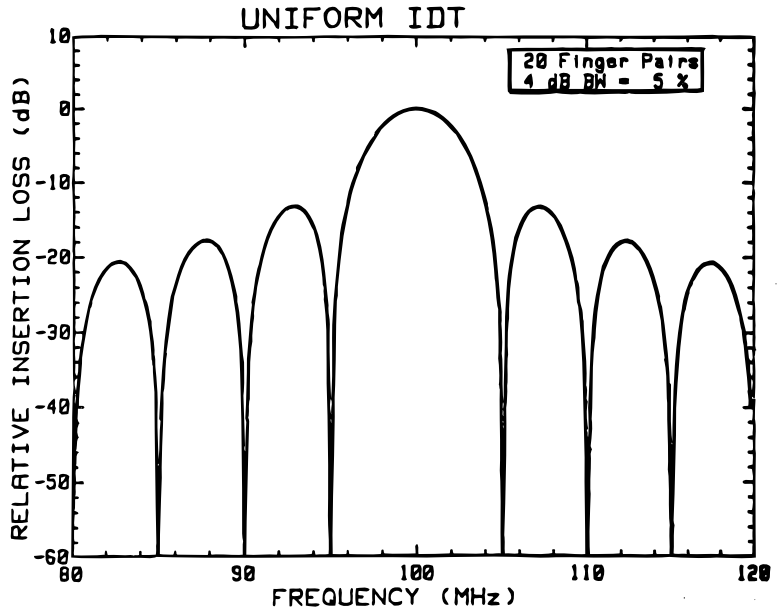


FIG. 3.5 Delta-function modeling of magnitude response $|H_1(f)|$ of illustrative uniform IDT with $N_p$=20 finger pairs, and center frequency $f_0 = 100$ MHz.[15]

## 3.4. FOURIER TRANSFORM PAIRS

Consider the relationship between the frequency response and the impulse response of a SAW filter. The impulse response is related to the frequency response by the Fourier-transform pair

$$H(f) = \int_{-\infty}^{+\infty} h(t)e^{-j2\pi ft}\,dt \tag{3.6a}$$

with a one-to-one correspondence between $h(t)$ and $H(f)$, where $h(t)$ is the impulse response and $H(f)$ is the frequency response of the system.

$$h(t) = \int_{-\infty}^{+\infty} H(f) e^{j2\pi f t}\, df \tag{3.6b}$$

Knowledge of one response enables the other to be derived. Starting with the desired steady-state frequency response, the corresponding impulse response can be derived and this result can be used to synthesize the geometric pattern of the impulse response, converted to the spatial domain. Let the desired transducer impulse response $h(t)$ be expressed as

$$h(t) = a(t) e^{j\varphi t} \tag{3.7}$$

where $a(t)$ is the time-dependent amplitude response. The phase-weighting condition, which tells us that the IDT fingers can only be placed at physically *real* locations, leads to the requirement that the phase $\varphi$ is

$$\varphi(t_n) = 0 \; or \; \pi \tag{3.8}$$

If we arbitrarily assume that the physical sampling is at the center of a finger gap, as shown in Fig. 3.6, Eq. (3.8) yields the required sampling times, and positions for each IDT finger. This is for the general case where the IDTs can have varying electrode spacing. For the uniform IDTs considered in this chapter the sampling period will, of course, be constant.

Particularly useful Fourier transform pairs to consider for SAW filter design are those relating to sinc-function responses in Fig. 3.7 are as applicable bandpass situations considered here. Observe that the time-domain amplitude response of Fig. 3.7 now becomes the modulation envelope in Fig. 3.8, while the zero frequency point translates to the carrier frequency.

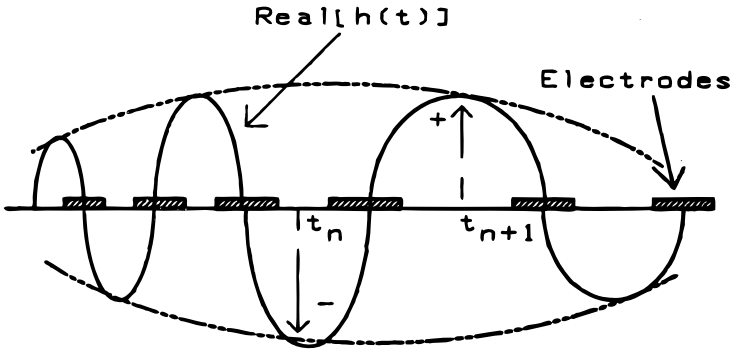


FIG 3.6. Relationship between sampling times and electrode-finger placement

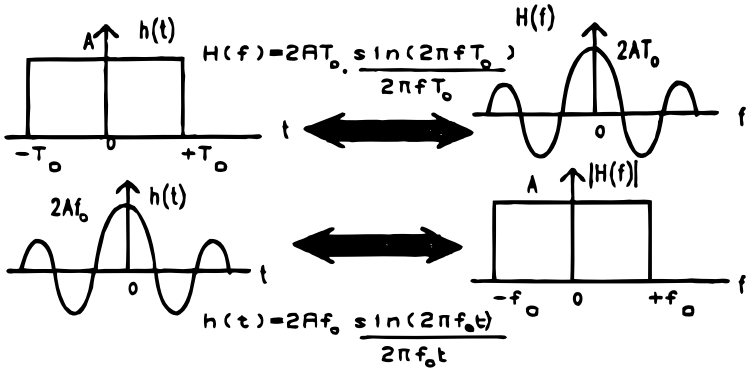


FIG 3.7. Baseband transformation for Fourier-transform pairs involving the sinc function in the time and frequency domains.

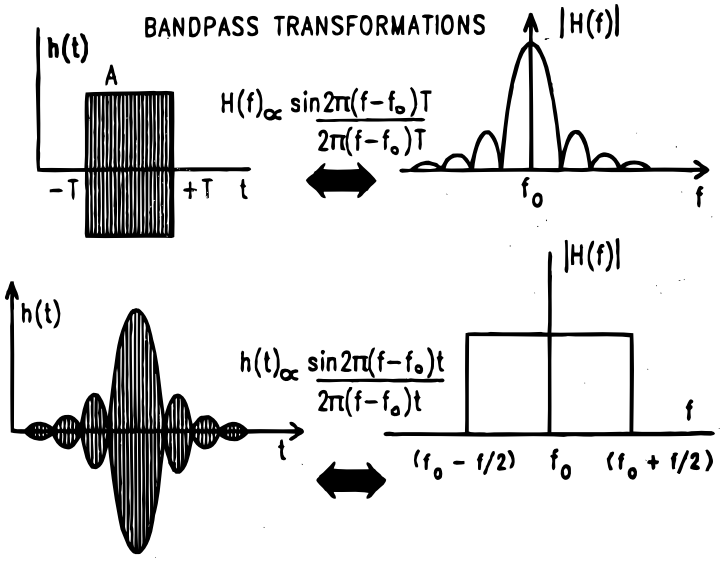


FIG 3.8. Bandpass transformations for Fourier-transform pairs involving the sinc function in the time and frequency domains.[15]

## 3.5. IMPULSE RESPONSE AND SAW FILTER APODIZATION GEOMETRY

The geometric pattern of an IDT is a unique feature of SAW filter design. It corresponds to spatially sampled replica of the IDT impulse response. The rationale behind the introduction of Fourier transform concepts now becomes apparent. To appreciate this concept, the reader should reexamine the illustrative sinc-function IDT with constant finger overlap in Fig. 3.4. Now compare these with the Fourier transform relations in Fig. 3.8. While the two responses have approximately the same shapes, there are two significant points of departure. With careful design, however, these can be accommodated to implement SAW filters with excellent agreement between theoretical and experimental responses. To elaborate on the preceding points, note first of all that the integration limits in the analog relationships of Eq. (3.6) extend to infinity. However, the impulse response of a SAW filter does not have infinite time duration. It lasts for only as long as the time taken for surface waves to propagate under the entire length of an IDT. In SAW filters, this will range from nanoseconds to microseconds, depending on the length of the IDTs. This is one source of approximation when designing SAW filters with recourse to the Fourier transform relations of Eq. (3.6). While the degree of correspondence will increase with the length of the IDT, some design trade-offs may be applied at this stage if the size substrate size and cost are to be kept within given constraints. On a second point of departure, the Fourier-transform relations in Eq. (3.6) relate to a continuously changing impulse response. Again, however, this is not the case for SAW filters, because the IDT fingers and their placement only give a spatially sampled approximation to the desired time domain impulse response of the analog SAW filter.

## 3.6. SINC FUNCTION APODIZATION OF THE IDT

Instead of using the uniform IDT of Fig. 3.4 with constant finger overlap apodization, consider what the effect will be on its frequency response if it is now given a sinc function apodization as sketched in Fig. 3.9. It can be anticipated that the frequency response of the SAW filter were of infinite time duration. This is of course not the case in practice due to truncation by the ends of the IDT. In the absence of any external feedback, a SAW filter is a *finite impulse response* (FIR) device.

In Fourier series expansions, truncation of the number of terms gives rise to Gibb's phenomena. In SAW filter operation, this manifests as undesirable amplitude and phase ripples in the passband. The amplitude response also suffers an additional degradation in that the steepness of the transition at the band edges is reduced. This can lead to filter overlap with resultant interference in frequency division multiplexing channels.

Gibb's ripple effects are illustrated in Fig. 3.10, which shows the computed response of a sample IDT with uniform finger spacing and sinc function apodization. Here, the IDT was designed for operation about a center frequency $f_0$=100 MHz, with $N_p$=100 finger pairs. In this example, the sinc function apodization of

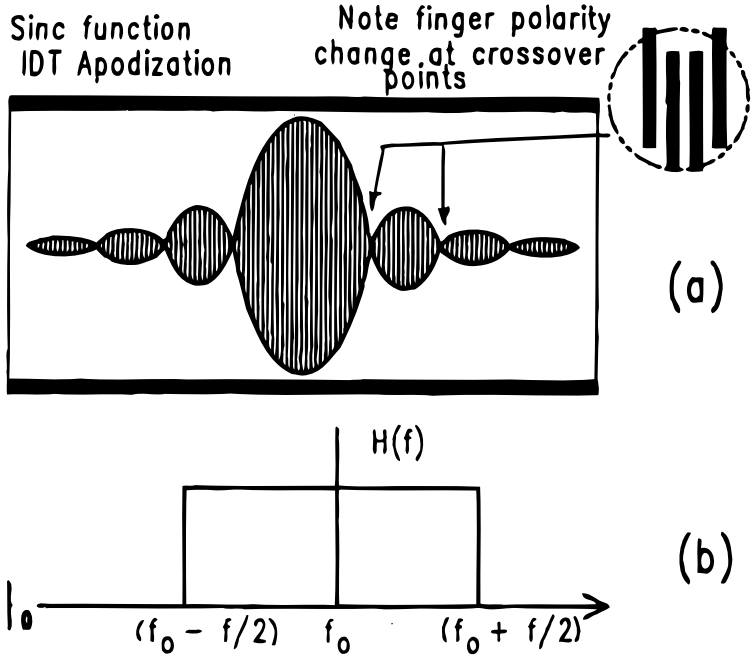


FIG 3.9. (a) IDT with sinc-function apodization of electrode-finger overlap. Note finger polarity changes as sinc function goes through zero crossings. (b) Ideal rectangular bandpass frequency response for sinc-function apodization extending to infinity along substrate propagation axis.[15]

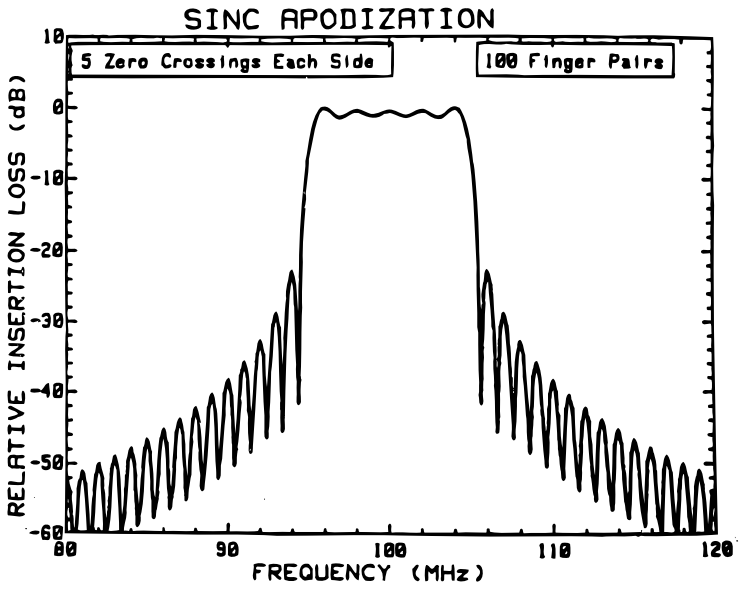


FIG 3.10. Example of amplitude of transfer-function response for IDT with sinc-function apodization extending to five zero-crossings on either side of main lobe of apodization pattern. The IDT has $N_p$=100 finger pairs, and $f_0$=100 MHz. Note Gibb's ripple in passband.[15]

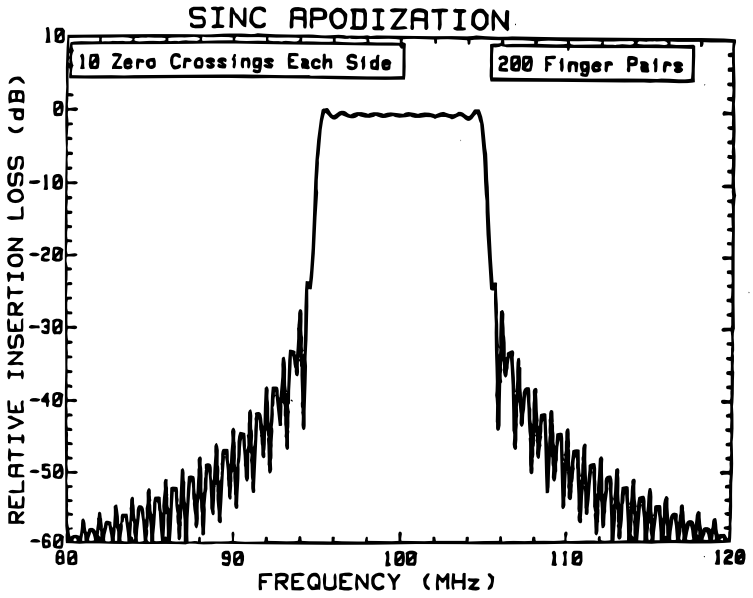


FIG 3.11. Gibb's ripple in the passband has same peak-to-peak amplitude but higher ripple frequency when sinc-function apodization of IDT pattern is extended to 10 zero-crossings, using longer IDT with $N_p$=200 finger pairs.[15]

the IDT pattern was truncated after only 5 zero crossings on eider side of the main lobe. Three undesirable features to note here are: (1) the Gibb's amplitude ripples in the passband, (2) the finite transition band, (3) the relatively poor close-in stopband rejection of ≈ 24dB. Figure 3.11 shows the computed passband response with the IDT length extended to $N_p$=200 finger pairs, with 10 zero crossings of the sinc function about the main lobe. Observe that the peak –to-peak amplitude ripple is about the same as in Fig. 3.10, although the ripple frequency has increased. There is, however, a noticeable decrease in the transition bandwidth as well as improvement in close-in sidelobe rejection from ≈ 24dB to ≈ 30dB. In both cases, computations of the frequency response obtained with delta function model.

## 3.7. CONVOLUTION AND WINDOW FUNCTION FOR SAW IDT's

The quality of a SAW linear-phase band-pass filter is determined mainly by three other parameters. These are: (a) peak-to-peak amplitude ripple in the passband, (b) the close-in sidelobe rejection, and (c) the group delay $\tau = -d\varphi/d\omega$, which gives the linearity of the phase response. Precision SAW bandpass filter specifications may call for amplitude ripples of less than 0.2 dB across the passband, close-in stopband rejections of greater than 50 dB and peak-to-peak group delay ripples of <5ns.

From Figs. 3.10 and 3.11 it was shown that increasing the length of an IDT with sinc function apodization improved its transfer function approximation to rectangular band-pass response. Given this situation, and neglecting second-order effects, how could an

extremely rectangular passband response be achieved without using excessively long apodized IDTs? The answer lies in the use of window function techniques, which modify the IDT apodization pattern so as to achieve the desired passband response with IDTs of modest length. Window functions are widely used in digital filter design to improve the shape of the passband response. The response of a digital FIR has but a finite length, due to the finite number of registers that store the impulse response coefficients. Finite impulse response length corresponds to the truncation of an infinite Fourier series. The abrupt truncation of a Fourier series gives rise to the Gibb's ripple phenomena considered above. In the bandpass amplitude response, this is evidenced as an overshoot followed by a periodic ripple as illustrated in Figs. 3.10 and 3.11.

Window function techniques involve convolution of two time-domain signals or two frequency response functions. To explain briefly the convolution process, consider operation in the time domain with two signals given by $f_1(t)$ and $f_1(t)$. The integral

$$f(t) = \int_{-\infty}^{+\infty} f_1(t) f_2(t-\tau) d\tau = f_1(t) \star f_1(t) \tag{3.9}$$

defines the convolution of $f_1(t)$and $f_2(t)$. The right-handed side of Eq. (3.9) is a symbolic shorthand notation for the convolution integral, where symbol $\star$ signifies convolution.

While the convolution shown in Eq. (3.9) is carried out in the time domain, it can also be conducted in the frequency domain. Two important theorems result, namely

**1. Time-Convolution Theorem:** The time-domain convolution of functions $f_1(t)$ and $f_2(t)$ *corresponds* to multiplication of their respective frequency responses $F_1(\omega)$ and $F_2(\omega)$. That is, if

$$f_1(t) \leftrightarrow F_1(\omega) \text{ and } f_2(t) \leftrightarrow F_2(\omega),$$

the Fourier transform of convolution integral $f(t)$ in Eq. (3.9) is

$$\mathcal{F}[f_1(t) \star f_2(t)] = F_1(\omega) F_2(\omega) \tag{3.10}$$

where $\mathcal{F}$ indicates the Fourier transform operation.

2. Frequency-Convolution Theorem: Convolution of the two responses $F_1(\omega)$ and $F_2(\omega)$ in the frequency domain responses $f_1(t)$ and $f_2(t)$.

In Eqs. (3.9) and (3.10) no restrictions have been placed on the forms of signals $f_1(t) and\ f_2(t)$. Either or both can represent impulse responses, in which case they can represented by $h_1(t)$ and $h_2(t)$, while the frequency responses $F(f)$, $F(\omega)$ can be replaced by $H(f)$, $H(\omega)$ in the notation of this text. In simple terms, the convolution process of Eq. (3.9) just represents a folding over of one of the responses (as given by the

minus sign in the –τ term), together with a relative time displacement of one of the responses by amount τ, followed by multiplication to get the overlap areas (as given by the integration symbol).

The IDTs of all SAW filters have a "built-in" window function. This is just the "rectangular" window function associated with the finite physical length of the IDT on the piezoelectric substrate. This shows time-and frequency-domain convolution equivalences with this rectangular window function. The time-domain here corresponds to the spatial domain of the IDT. The resultant Gibbs' oscillation in the overall bandpass response appears in the bottom-left illustration. Now consider the example of Fig. 3.17, where a cosine window function has additionally been included to modify IDT apodization. Here, the "product" window function is (built-in rectangular window)×(cosine window)=(cosine window). At the corresponding cosine-window value, to give the resultant apodization overlap length for that finger.

## 3.8. OVERALL SAW FILTER RESPONSE

As far only the response $H_1(f)$ of one IDT has been considered. The overall response $H(f) = H_1(f) \cdot H^*{}_2(f)$ may be readily determined by including the response $H_2(f)$ of the second IDT. (The notation $H^*{}_2(f)$ in the previous sentence just means the complex conjugate of $H_2(f)$.) This should simply be a wideband IDT with relatively few finger pairs, so that it does not degrade the desired bandpass response design incorporated into $H_1(f)$. Figure 3.12 shows the computed SAW filter response with a wideband output IDT used in conjunction with the cosine-weighted IDT. By contrast, Fig 3.13 shows the reduced performance that results if the bandwidth of the output IDT is made too narrow for the desired response.

It should be observed that SAW filters are reciprocal devices in that it does not matter (theoretically) which IDT is used as the input one. In practice, however, there will generally be some observable difference in response, depending on the degree of mismatch between the impedance of each IDT and the load or source resistance to which it is attached.

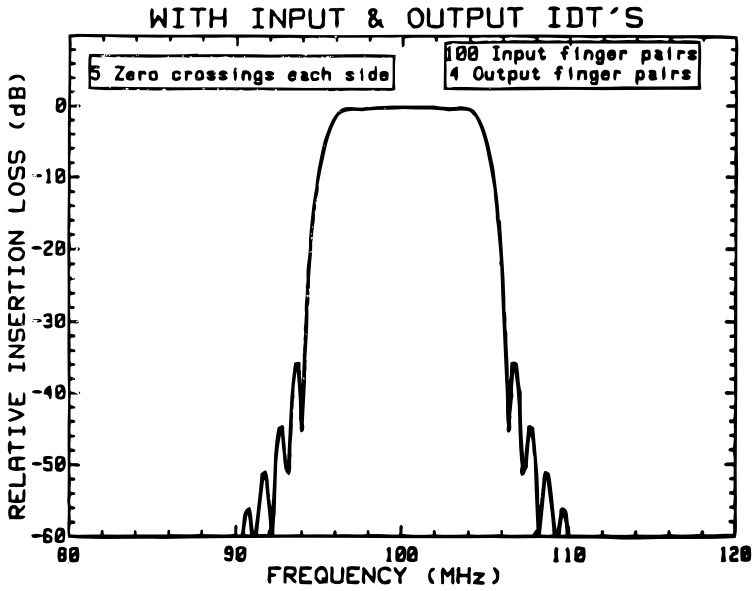


FIG 3.12. Delta-function model used to calculate overall amplitude response of 100-MHz SAW filter using cosine-weighted IDT of Fig. 3.17 as the input IDT, with broadband IDT as receiver. Input IDT has $N_p$ =100 finger pairs with sinc function apodization and cosine-weighting. Uniform output IDT has $N_p$ =4.[15]

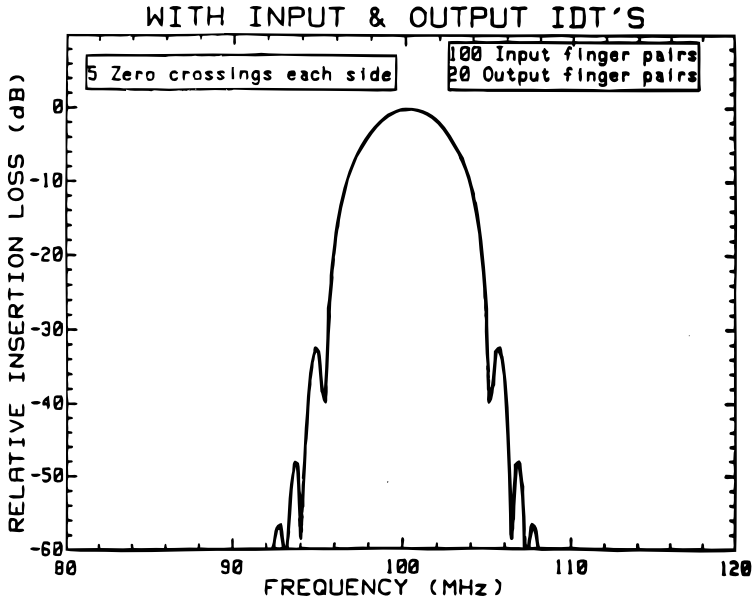


FIG 3.13. Degradation of overall response of the 100-MHz filter when the output IDT is made too marrowband. Input IDT again has *Np* =100 finger pairs, but output IDT now has *Np* =20 finger pairs.[15]

## 3.9. THE DELTA FUNCTION MODEL

The delta-function model is the simplest of the various models that describe the performance of a bidirectional SAW IDT. Although it is normally applied to IDTs with uniform finger spacings and constant and constant or varying apodization overlap, it can also be

applied to simple modeling of chirp filters with non-uniform IDTs. It can also be used to model relative degradation of passband response due to triple-transit-interference and/or electromagnetic feedthrough. Its major limitation is that it cannot be applied to obtain absolute insertion loss values because it has no provision for handling impedance levels. Despite this, it can be excellent for modeling frequency response in preliminary designs. The delta-function model is really a representation of an ideal transversal filter sketched in Fig 3.14. In the time domain, the output $y(t)$ of this filter is the superposition of the weighted outputs of a series of delay elements subjected to an input stimulus $x(t)$. For delay elements, the output is

$$y(t) = \sum_{n=1}^{N} A_n x(t - T_n) \tag{3.11}$$

In terms of SAW IDT parameters, $A_n$ corresponds to the finger overlap of the *n*th finger pair, while $T_n$ is the accumulative delay time for the SAW to traverse to the *n*th finger pair. For a finite number *N* of such finger pairs, this filter has finite impulse response (FIR). It will be a stable system (in the absence of feedback) because its impulse response *h(t)* will be absolutely integrable (i.e. $\int h(t)dt < \infty$ when integrated over all time).

A shift in the time domain corresponds to a multiplication by $e^{-j\omega T_n}$ in translating to the frequency domain, so that the output frequency response *Y(ω)* is given by

$$y(t) = \sum_{n=1}^{N} A_n \int_{-\infty}^{\infty} x(t - T_n)\, e^{-j\omega T_n} dt = \sum_{n=1}^{N} A_n\, e^{-j\omega T_n} X(\omega) \tag{3.12a}$$

$$Y(\omega) = H(\omega)X(\omega) \tag{3.12b}$$

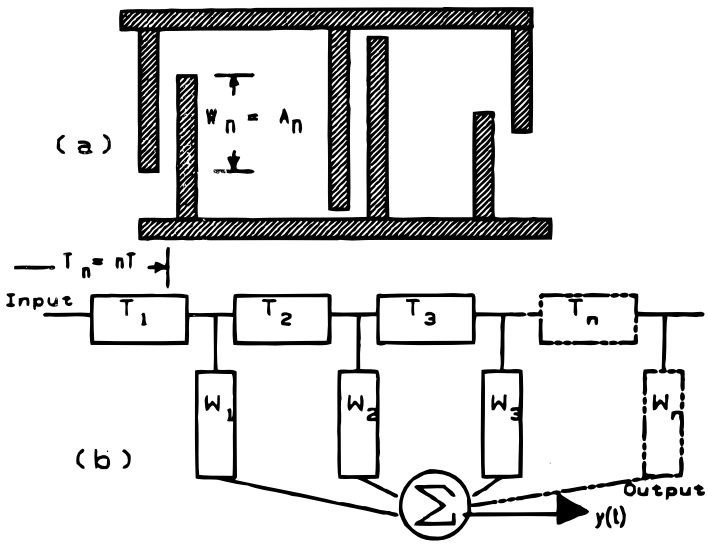


FIG 3.14. (a) Finger placement and apodization of an IDT. (b) Transversal filter equivalent-circuit representation.[15]

where $Y(\omega)$ is the Fourier transform of $y(t)$ and $X(\omega)$ is the Fourier transform of $x(t)$. From Eq. (3.12a), the frequency response $H(\omega)$ of the transversal filter is

$$H(\omega) = \sum_{n=1}^{N} A_n \, e^{-j\omega T_n} \tag{3.13}$$

where $T_n = nT$ for uniform finger spacing, and $A_n = a_n e^{j\varphi}$. Equation (3.13) corresponds to the delta-model formulation given in Eq. (3.12).

## 3.10. THE CROSS FIELD MODEL

The SAW *cross-field model* is derived from the Mason equivalent circuit employed for modeling acoustic *bulk* wave piezoelectric devices. In this model the electric field distribution under the electrodes of an excited IDT is approximated as being normal to the piezoelectric surface, as if between the plates of a capacitor, as sketched in Fig. 3.15(a). An alternative model known as the *in-line* model is given in Fig. 3.15(b) for reference.

In the adaptation of the Mason equivalent circuit to SAW filter design, each IDT is represented by a three-port network, shown in Fig. 3.16. In the terminology followed here, Ports 1 and 2 represent electrical equivalents of “acoustic” ports, while Port 3 is a true electrical port. The electrical equivalents in Ports 1 and 2 are those for an acoustic, and passive, SAW transmission line. Port 3 is where the actual signal voltages are applied or detected.

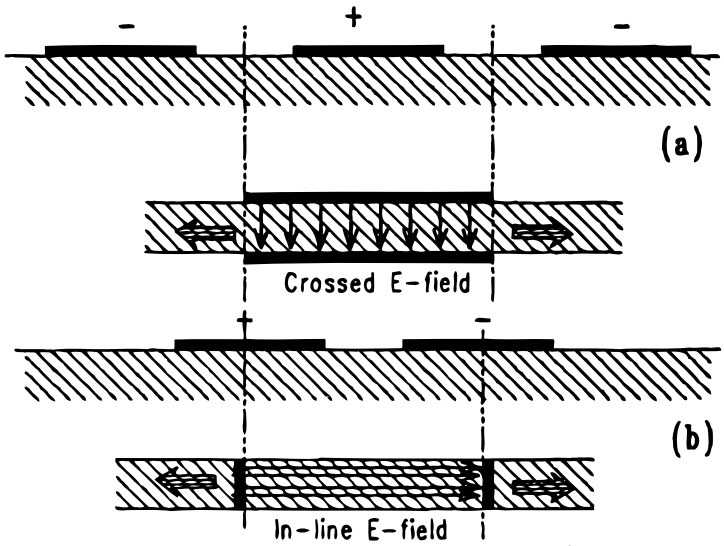


FIG 3.15. Simplistic representations depicting: (a) an instantaneous *E*-field direction in the crossed-field model, and (b) an instantaneous *E*-field distribution for the "in-line" model.[15]

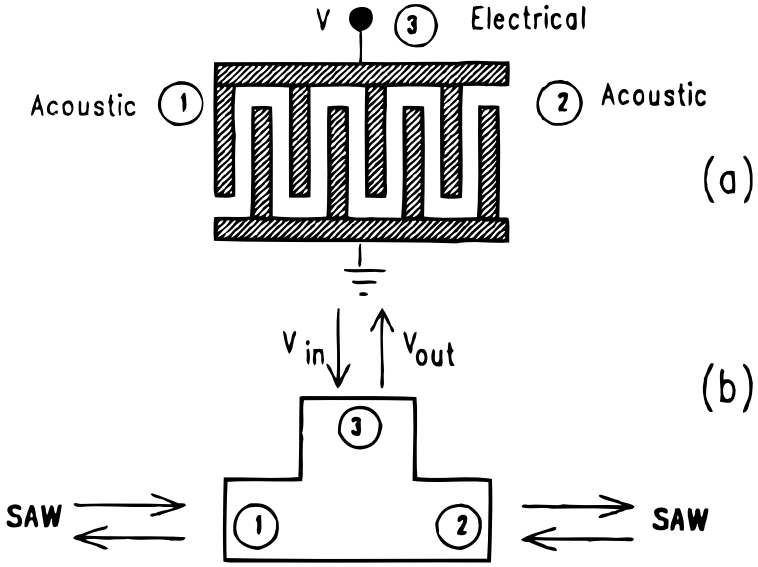


FIG 3.10.2. (a) Representation of the SAW IDT as a three-port network, Ports 1 and 2 are normally assigned to the "acoustic" ports, while Port 3 is the electrical port. (b) In the cross-field model, acoustic signals at Port 1 and 2 are converted to equivalent electrical transmission-line parameters.[15]

It should be noted that all of the subsequent derivations in this chapter apply to an IDT where acoustic reflections from IDT finger discontinuities are neglected. This approximation can be considered to hold for electrodes with low values of film-thickness ratio ($h/\lambda \ll \sim 1\%$). As will be seen, the result of making this approximation is that the radiation conductance parameter $G_a(f)$ to be derived will have a sinc-function (symmetric) amplitude response about center frequency.

For all three ports to be treated in equivalent electrical terms, the acoustic parameters at Ports 1 and 2 must be converted to electrical equivalents. At these ports acoustic forces $F$ (in newtons) are transformed to electrical equivalent voltages $V$, while mechanical SAW velocities $v$ are transformed to equivalent currents $I$. In terms of a common proportionality constant $\varphi$ these transforms are

$$V = F/\varphi \qquad (3.14a)$$
$$I = v\varphi$$

where parameter $\varphi$ is interpreted as the turns-ratio of an equivalent acoustic-to-electric transformer. In turn, these definitions allow the mechanical characteristic impedance $Z_m = F/v$ of the piezoelectric substrate to be expressed as an equivalent transmission line characteristic impedance $Z_0$.

For a uniform acoustic wave propagating in a substrate of density $\rho(kg/m^3)$ and large cross-sectional area $A(m^3)$, the mechanical impedance can be written as

$$Z_m = \rho v A \ (kg/s) \qquad (3.14b)$$

while the equivalent electrical characteristic impedance is

$$Z_0 = \frac{Z_m}{\varphi^2} \ (ohm) \qquad (3.15)$$

These definitions enable the electrical characteristic admittance $G_0 = 1/Z_0$ of the equivalent SAW transmission line to be derived as

$$G_0 = K^2 C_s f_0 \ (mho) \qquad (3.16)$$

where $K^2$=electromechanical coupling constant, $f_0$=IDT center frequency and $C_s$=static capacitance of one periodic section, $C_s$ may also be expressed as $C_s = C_0 W$, where $C_0$=capacitance/finger pair/unit length (pF/cm) and $W$= finger apodization overlap (cm).

In terms of a three-port admittance applicable to Fig. 3.17, the equivalent current-voltage relations for a single IDT are given as

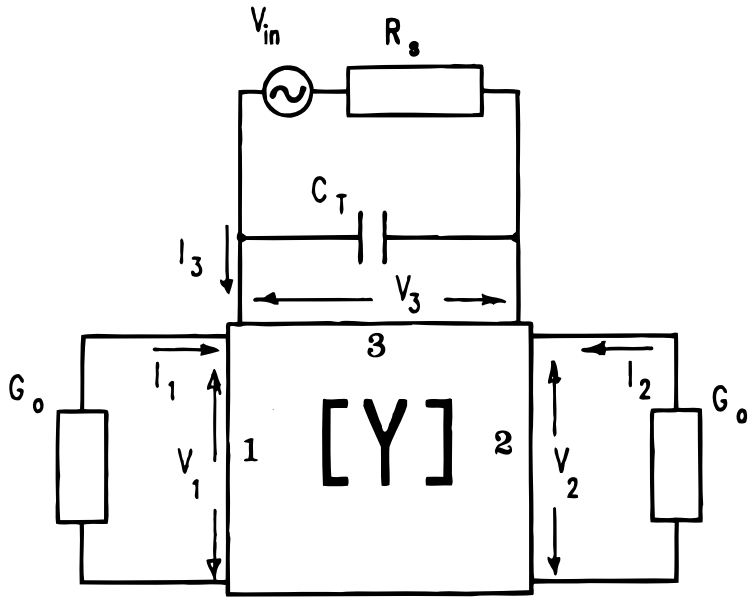


FIG 3.17. Three-port equivalent admittance network representation for an IDT in the cross-field model. Here $G_0$ is the equivalent electrical characteristic conductance of a SAW transmission line. The total IDT capacitance $C_\tau$ can be considered to be "outside" the remaining admittance configuration[15]

$$\begin{pmatrix} l_1 \\ l_2 \\ l_3 \end{pmatrix} = [Y] \begin{pmatrix} V_1 \\ V_2 \\ V_3 \end{pmatrix} \tag{3.17}$$

where the 3×3 admittance matrix $[Y]$ may be expanded as

$$[Y] = \begin{pmatrix} Y_{11} & Y_{12} & Y_{13} \\ Y_{21} & Y_{22} & Y_{23} \\ Y_{31} & Y_{23} & Y_{33} \end{pmatrix} \tag{3.18}$$

Under the notation used here, matrix subset elements $Y_{11}, Y_{12}, Y_{21}, Y_{22}$ are just those relating to an equivalent SAW transmission line.

A first stage of simplification can now be applied. From transmission-line symmetry and reciprocity, $Y_{11} = Y_{22}$ and $Y_{21} = Y_{12}$. An additional simplification can be applied to the remaining matrix elements involving electrical port 3, by setting $Y_{32} = -Y_{13}$. The negative sign is required here, because a voltage applied to port 3 causes a SAW to emanate from both sides of the IDT with the same potential Φ. With these simplifications, Eq. (3.18) reduces to

$$[Y] = \begin{pmatrix} Y_{11} & Y_{12} & Y_{13} \\ Y_{12} & Y_{11} & -Y_{13} \\ Y_{13} & -Y_{13} & Y_{33} \end{pmatrix} \tag{3.19}$$

These matrix elements for the crossed-field model may be derived to be

$$\begin{aligned} Y_{11} &= -jG_0\cot(N\theta) \\ Y_{12} &= jG_0\csc(N\theta) \\ Y_{13} &= -jG_0\tan(\theta/4) \\ Y_{33} &= j\omega C_T + j4NG_0\tan(\theta/4) \end{aligned} \tag{3.20}$$

where $G_0 = 1/Z_0$ =characteristic admittance (mho), $C_T = NC_s$ =total IDT capacitance $(F)$, $N$=number of electrode pairs (periods), $C_s$=capacitance of one finger pair $(F)$ and $\theta = 2\pi(f/f_0)$= electrical transit angle, in radians, through one electrode pair (i.e. one period).

Unfortunately, the matrix elements in Eq. (3.20) "blow up" at center frequency, when $\theta = 2\pi$. The impedance and transfer functions remain finite, however, and may be calculated by expanding the matrix for frequencies near center frequency. When this is done, the input admittance $Y_3$ at center frequency $f_0$ may be expressed as

$$Y_3(f_0) = \left.\frac{I_3}{V_3}\right|_{f_0} = G_a(f_0) + j2\pi f_0 C_T \tag{3.21}$$

where $G_a(f_0)$=the radiation conductance at center frequency $f_0$ such that

$$G_a(f_0) = 8K^2 f_0 C_s N^2 \ (mho) \tag{3.22}$$

However, from Eq. (3.16) the equivalent characteristic admittance $G_0$ of the SAW transmission line is given as $G_0 = K^2 C_s f_0$. This can be substituted in Eq. (3.22), to give the input radiation conductance at center frequency as

$$G_a(f_0) = 8N^2 G_0 \ (mho) \tag{3.23}$$

For frequencies near center frequency Eq. (3.23) may be generalized as

$$\begin{aligned} G_a(f) &= G_a(f_0)\left|\frac{sinx}{x}\right|^2 \\ &\approx 8N^2 G_0\left|\frac{sinx}{x}\right|^2 : \text{(neglecting IDT finger reflections)} \end{aligned} \tag{3.24}$$

where $x = N\pi(f - f_0)/f_0$ in the unperturbated sinc-function relation $sinc(X) = (sinX)/X$, which does not incorporate effects of acoustic reflections at IDT finger discontinuities.

Equation (3.21) may be also generalized as

$$Y_3(f) = G_a(f) + j2\pi f C_T \ (mho) \tag{3.25}$$

in approximating the input admittance.

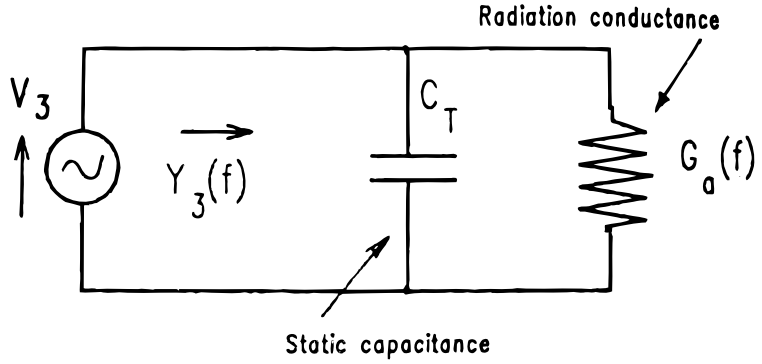


FIG 3.18. Crossed-field equivalent admittance at electrical Port 3, for an IDT at center frequency. Imaginary conductance $G_a(f)$ relates power generation from an excited IDT. (Analogous to radiation resistance in an electromagnetic antenna.) $C_T$ is the total static of IDT. Radiation susceptance $B_a(f) = 0$.[15]

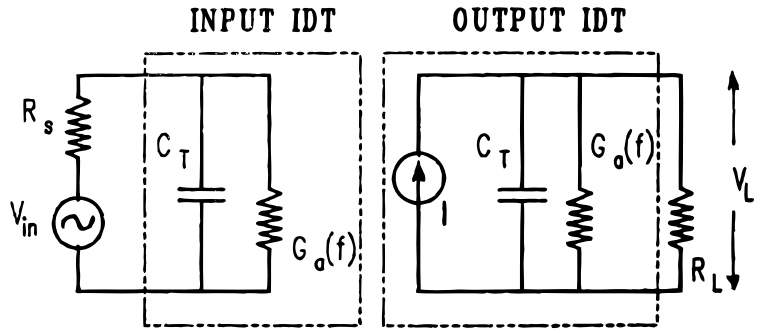


FIG 3.19. Input/output equivalent circuit for a SAW filter in the crossed-field model. Output IDT is considered to be excited by a high-impedance current source proportional to the SAW amplitude. Here, $R_S$ and $R_L$ are the filter source and load resistances.[15]

The equivalent circuit input impedance of Fig. 3.17 is sketched in Fig. 3.18. The same principles can be applied to model the output IDT. In this case, the equivalent excitation source for output IDT is a current source. (The use of a current source here can be deduced intuitively, since the output IDT can be visualized as “looking back” into a high impedance source.) the overall equivalent circuit of the SAW filter, including source and load impedances is then as sketched as in Fig. 3.19.

# SIMULATION

## 4.1. GEOMETRY DESIGN

This is a non-linear model with high requirements in computer hardware and computational time for a high detail simulation. One solution to speed up the process is to reduce the dimensions of the problem in various ways explained further in detail.

Only one wave length of the substrate is modeled. Due to the shape of the IDT arrays one dimension can be ignored thus a 2 Dimension model is used. All gradients in the third direction should be assumed to be zero. The depth of the substrate and the piezoelectric combined is limited to at least 7 wavelengths to limit the size of the problem. The size of the substrate and piezoelectric are constant but the height of the IDTs is variable.

A typical two port SAW resonator is on the order of 1000λ delay line (transducer and delay length) long, 500λ wide in the lateral direction (aperture) and a depth of up to 10λ as shown below. It is well known that the degree of discretization of the model is directly proportional to the accuracy of the results. In the problem of interest, at least 20 first order (linear) elements per wavelength would be required to get reasonably accurate results. Calculating optimistically, the total number of elements required for the whole device (without electrodes and reflectors) gives:

$$\text{Number of elements} = 1250 \times 500 \times 10 \times 20 = 1.25 \times 10^8$$

A piezoelectric problem has four degrees of freedom namely, displacement in X direction (Ux), displacement in Y direction (Uy), displacement in Z direction (Uz) and potential (φ). So the total number of unknowns can be calculated as:

$$\text{Total number of unknowns} = 1.25 \times 10^8 \times 4 = 5 \times 10^8$$

Clearly, this number of equations would need to be solved in order to arrive at a complete solution. Also, it should be kept in mind that this is a conservative estimate and the actual number could be much more if we take into account the IDT, reflectors and more accuracy. Solving these equations is possible only by powerful super computers whose cost and time required (to solve) is not justified. Some valid approximations are required to reduce the size of the model to a manageable level.

The dimensions of the simulated models are Si substrate height 10 μm, GaN piezoelectric layer height 1.6 μm and IDT electrode height 80 nm. The width of the IDT electrodes was 130 nm and 200 nm, the wavelength was 260 nm and 400 nm respectively for the Single-electrode but for the DART and Split-electrode type only 200 nm finger width was used with wavelength 800 nm, four times larger than finger width because the periodicity is four IDTs. Below in Fig 4.1 are shown the Single-electrode and Split-finger type IDTs with their dimentions.

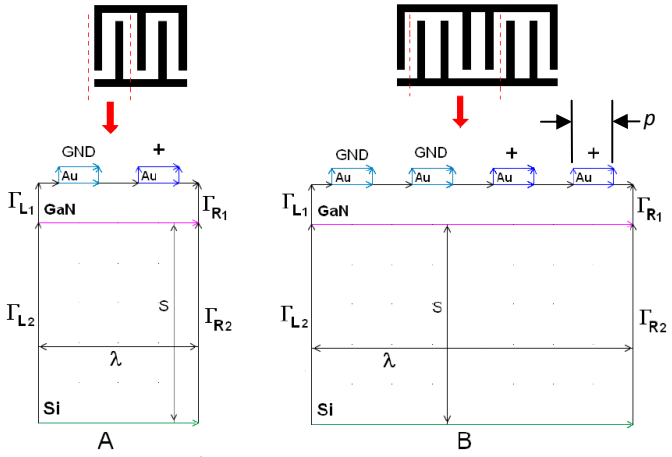


Fig 4.1. On the top is the "top view" of the IDTs with two periods and bottom is the cross-section of the Single-electrode and Split-electrode type IDT dimensions of the substrate the piezoelectric layer and the IDT fingers.[2]

## 4.2. BOUNDARY CONDITIONS

In order to have finite element solutions, boundary conditions must be applied precisely. Periodic boundary conditions are defined on both sides of the substrate. No mechanical constraints should be on the surface, thus stress-free boundary conditions are specified at the top of the substrate and the electrodes. Both piezoelectric and the substrate have "zero charge/symmetry" electric boundary conditions, but electrodes are grounded or have 1 Volt electric potential accordingly to the examined type of the model (normal, Split-electrode, DART).

## 4.3. SUBDOMAIN

The substrate material used is Silicon (Si), the piezoelectric material is Gallium Nitride (GaN) and the electrodes are made of Gold (Au). Material properties for substrate and piezoelectric GaN layer are defined by the crystal cuts of the wafer so the input constants are in matrix order described at the constants chapter. Properties such as Young modulus, Poisson's ratio, density, thickness, elasticity matrix, coupling matrix, relative permittivity, and electric conductivity are also defined.

## 4.4. MESH

In the finite element method, the problem domain is discretized into smaller regions called elements which are connected at specific points called nodes. The elements created may be two or three dimensional and can be triangular and quadrilateral. The solutions to the unknowns (field variables such as displacement, potential, stress, etc) are determined at these nodes and these unknowns are degrees of freedom (DOF). The continuum has infinite degrees of freedom, whereas the discretized domain has finite number of DOFs, contributing to the name finite element

The detail of the mesh has a major effect in simulation/computation time. Finer the mesh, mesh cluster number increases and more equations have to be solved. On the surface the displacement has the largest value and taking this into consideration a dense mesh is defined for the top layers, for higher accuracy measurements and a less dense mesh is defined at the lower layers, in order to reduce the number of the equations of the simulation. The domain is discretized to higher densities near the area of interest. Meshing density is decreasing moving towards the substrate. The number of triangular elements used is 1000, generating a system of 1000 degrees of freedom (dots).

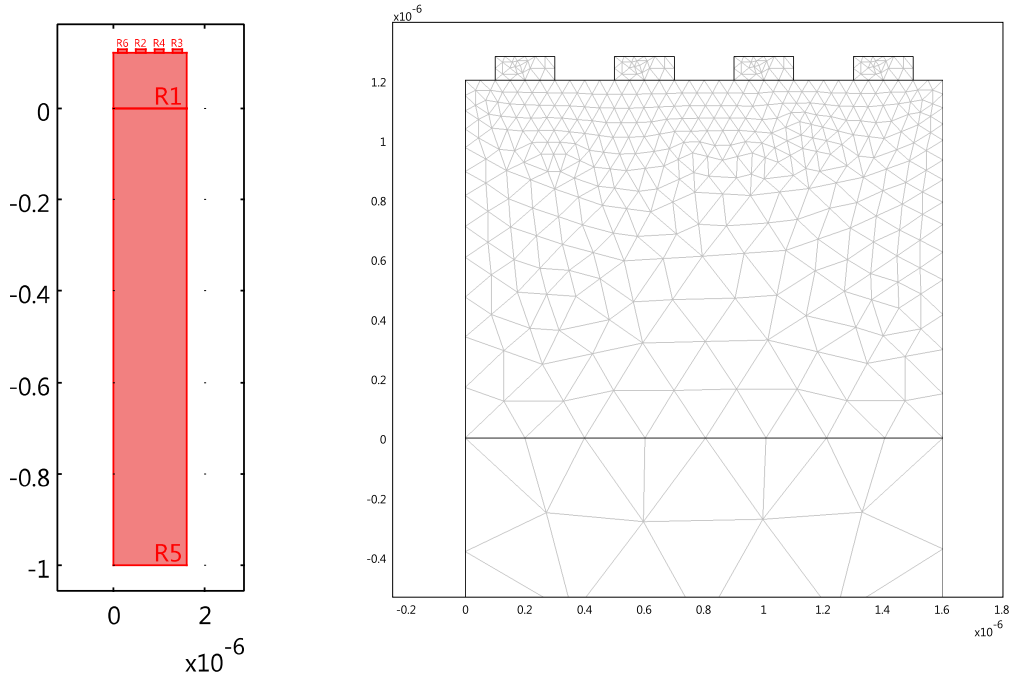


(a) (b)

Fig 4.2. The geometry (a) and the discretization (b) (zoomed) of the simulated structures.

## 4.5. SIMULATION RESULTS

Frequency domain solver is employed in the simulations. The geometrical parameters valued in the simulations are: IDT height, IDT width and substrate height. As shown below these variations change the equations and can have a big impact in the frequency response.

## 4.6. IDT HEIGHT

The highest of the IDT fingers influence the frequency response. A shift of the resonance frequency is observed when changing the IDT height. It seems that the electrons have a

higher movement freedom in an IDT with a wider cross-section because it has lower resistivity and this affects the frequency as the substrate comes to resonance.

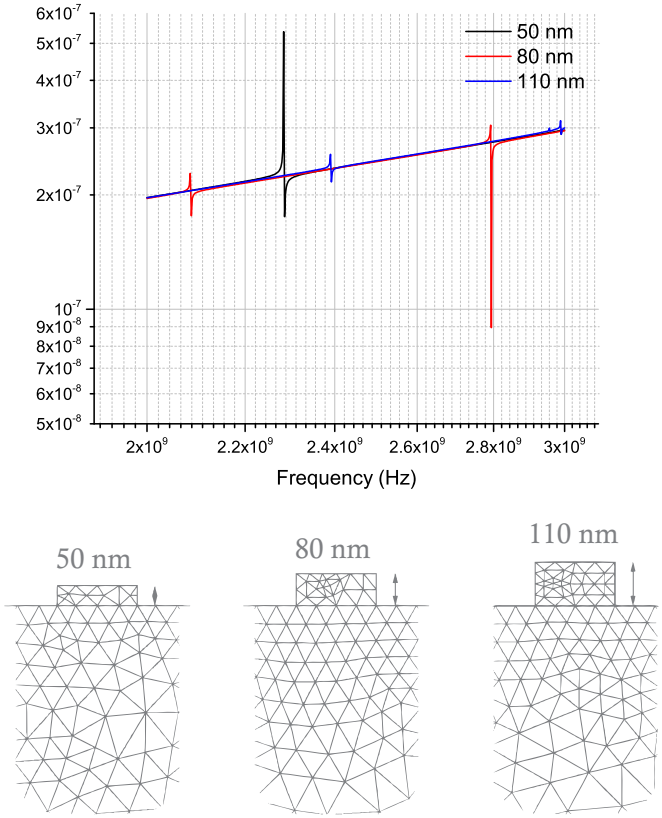


Fig 4.3. Frequency response comparison between different IDT heights.

In order to accurately compare the results obtained when the height of IDT is changed a mesh having the same element size should be employed.

## 4.7. SUBSTRATE HEIGHT

In SAW devices the amplitude of the acoustic wave is decreasing along with the distance to the substrate. The minimum height of the substrate (substrate + piezoelectric) used in the simulations is seven times the length of the desired acoustic wave.

As seen in Fig 4.4 the height of the substrate can affect the amplitude of the resonant frequencies. At resonant frequency the amplitude of the vibration is getting larger the higher the substrate width is, for up to 10 times the resonant wave length.

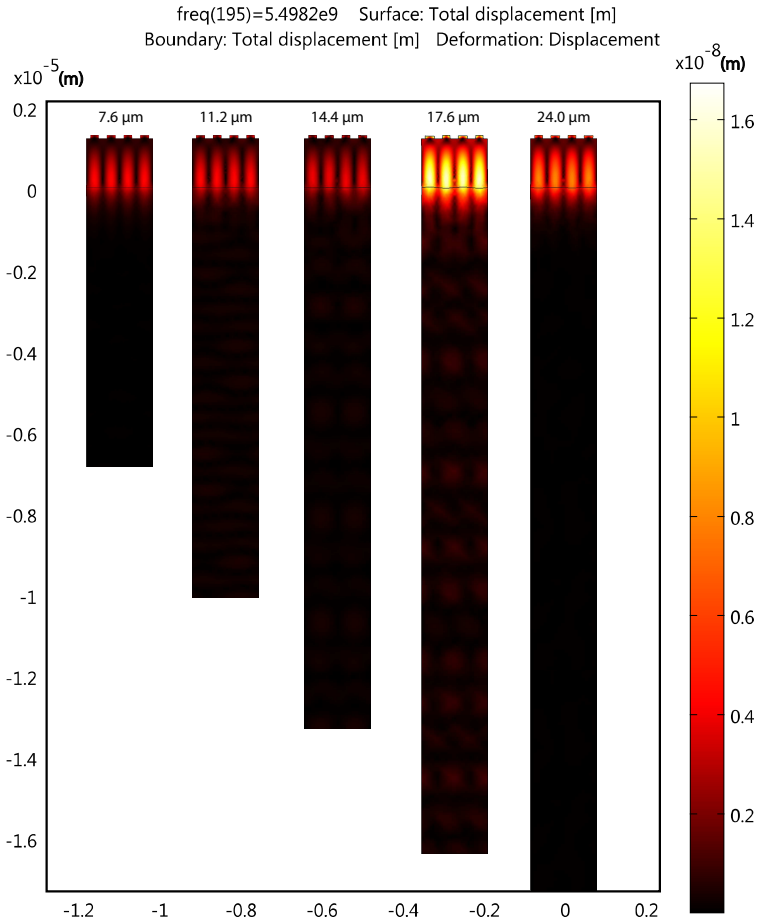


Fig 4.4. Displacement at resonant frequency for variable substrate heights equal to a multiple of wave length for constant IDT parameters.

As mentioned above, a slight change in the mesh can cause a considerable difference in the results. This makes it difficult to have an accurate comparison for the amplitude. For heights of small multiples of the resonant wavelength the amplitude has linear increase. For substrate heights more than 10 resonant wavelengths the amplitude seems to have reached maximum value, thus remains almost constant.

## 4.8. SPLIT-ELECTRODE IDT

A standard technique employed to reduce undesirable finger reflection effects involves the use of IDTs with split-electrode geometries, as shown in Fig. 6.14. As illustrated in Fig. 4.6, for electrode widths and spacing of $\lambda_0/8$ at center frequency, differential path lengths are such that the SAW reflections from each split-electrode pair cancel out at center frequency, rather than add on as for single-electrode IDTs[34].

One disadvantage of the split-electrode geometry is in the increased lithographic resolution required for fabricating IDTs. For SAW filters operating in the fundamental mode, this means that if the maximum attainable device frequency with single-electrode IDTs is 1 GHz, using a sophisticated photolithographic camera, the same photography can yield only split-electrode IDTs operating at maximum fundamental frequencies of 500 MHz. In some instances this problem may circumvent by operating the IDTs in a harmonic mode[35].

Two other design IDT design parameters may change with the use of split-electrodes structures. First of all, the effective electromechanical coupling coefficient $K_e^2$ is not the same as for single electrodes[36]. In addition, the capacitance $C_T$ of a split-electrode IDT is 1.4 times larger than for an equivalent single-electrode one[37].

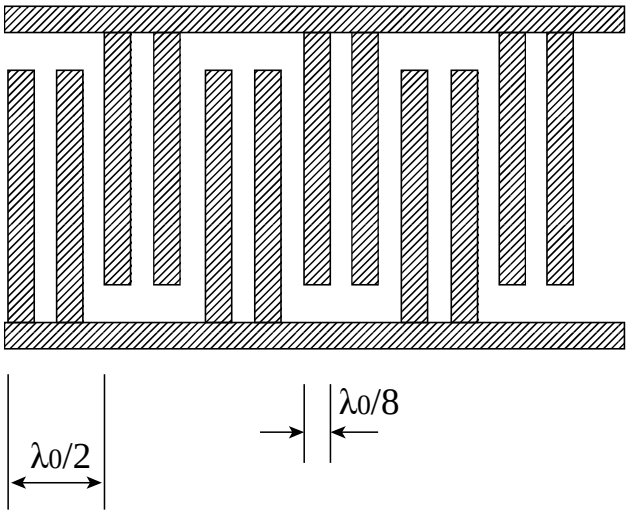


Fig. 4.5 IDT with split-electrode geometry and metallization ratio $\eta=0.5$.

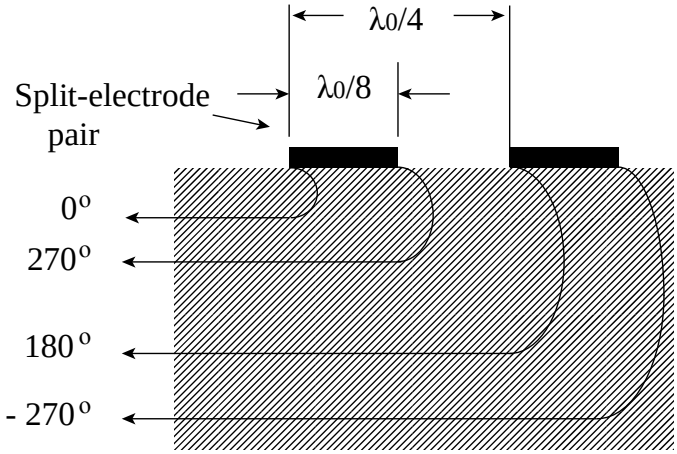


Fig. 4.6 SAW reflections from edges of split electrodes give a resultant minimum at center frequency. Used in filter designs where IDT finger reflections are undesirable.

## 4.9. DART (Distributed Acoustic Reflection Transducer)

The DART is a type of single-phase unidirectional transducer (SPUDT) introduced by Kodama et al[30] and now well established for I.F. filter applications[38].
In its basic unweighted form each period consists of two narrow electrodes and one wide electrode, as in Fig. 1a. The reflection center can be seen to be at the center of the wide electrode, because this is a center of symmetry when the bus bars are shorted. To a good approximation, reflections from the narrow electrodes can be ignored because they occur in pairs spaced such that the reflections cancel at the center frequency. Hence the wide electrode can be regarded as the reflector[27]

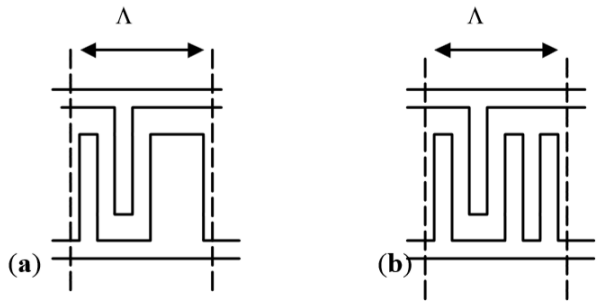


Fig.4.7. (a) DART structure, 1 period. (b) the same with reflection removed.

## 4.10. IDT WIDTH

As explained in theory, one parameter that defines the acoustic wave length and the resonant frequency is the IDT width. In the following simulations two different IDT widths have been examined 200 nm and 130 nm. Each one gives a resonant frequency, defined by the acoustic wavelength, and also other minor resonances in different frequencies.

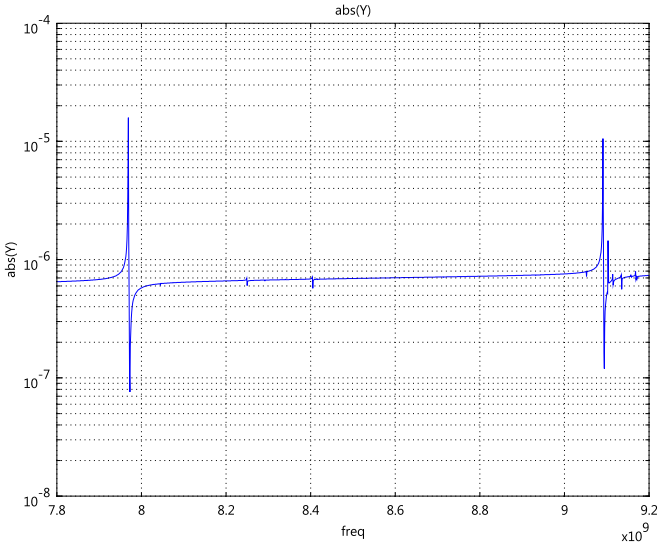


FIG 4.9. Frequency response of SAW device with IDT finger width 130 nm.

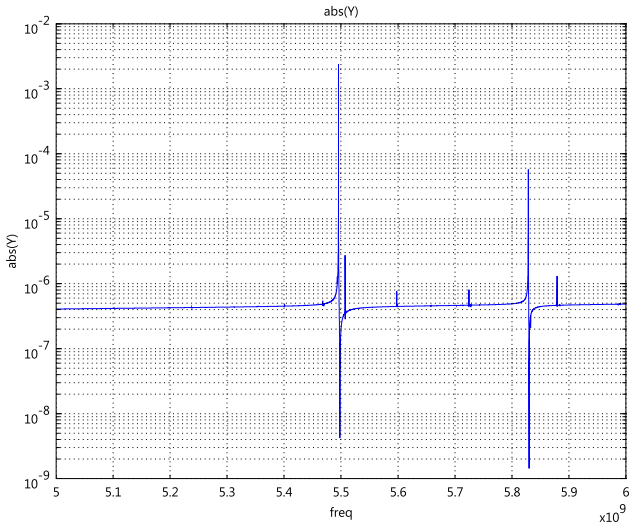


FIG 4.10. Frequency response of SAW devices with IDT width 200 nm.

On the below color figures, total deformation is shown with the outline of the device, surface colors represent the electric potential and a scale is drawn on the right side, and the arrows describe the direction and the magnitude of the electric field.

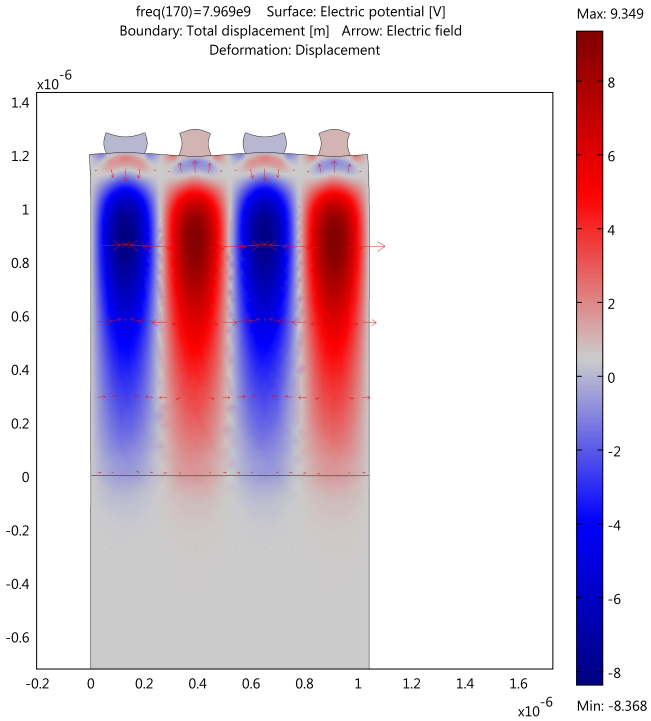


Fig 4.11 Electric potential of a SAW device of 130 nm IDT width, with resonance at 7.969 GHz.

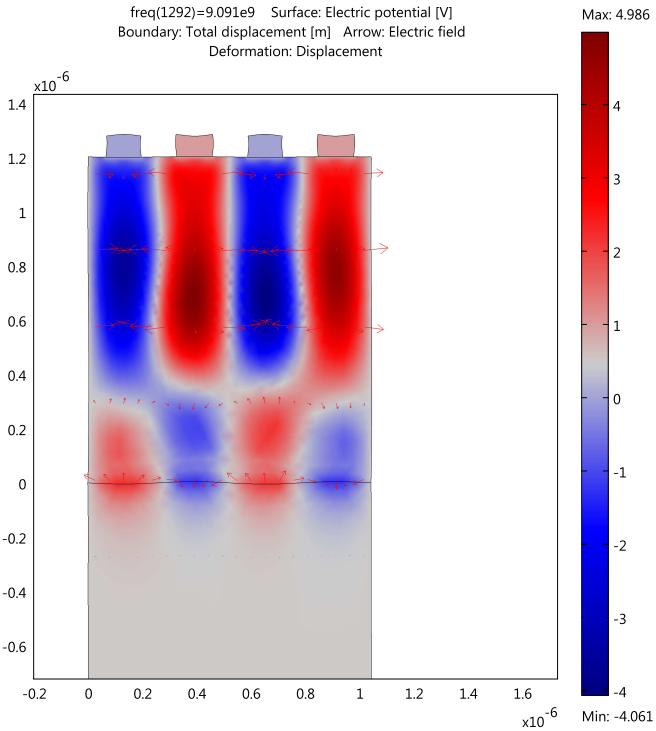


Fig 4.12. Electric potential of a SAW device of 130 nm IDT width, with resonance at 9.091 GHz.

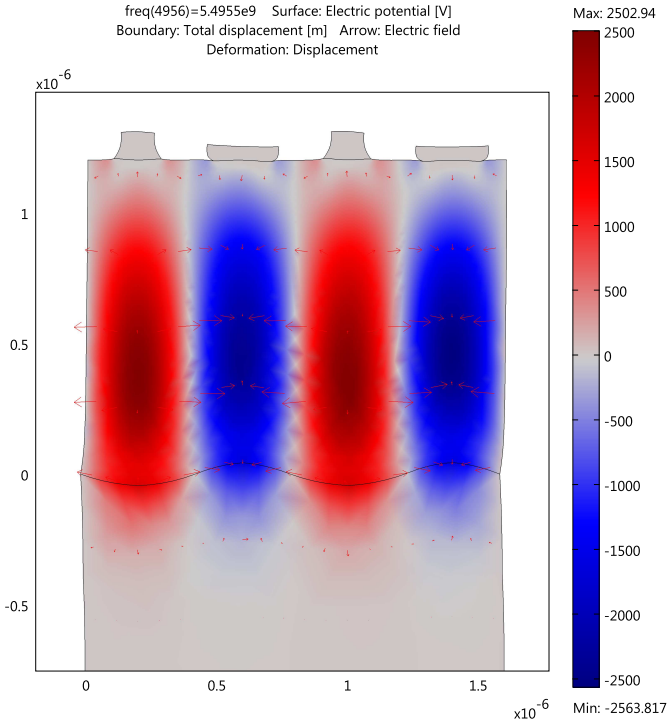


Fig 4.13. Electric potential of a SAW device of 200 nm IDT width, with resonance at 5.4955 GHz.

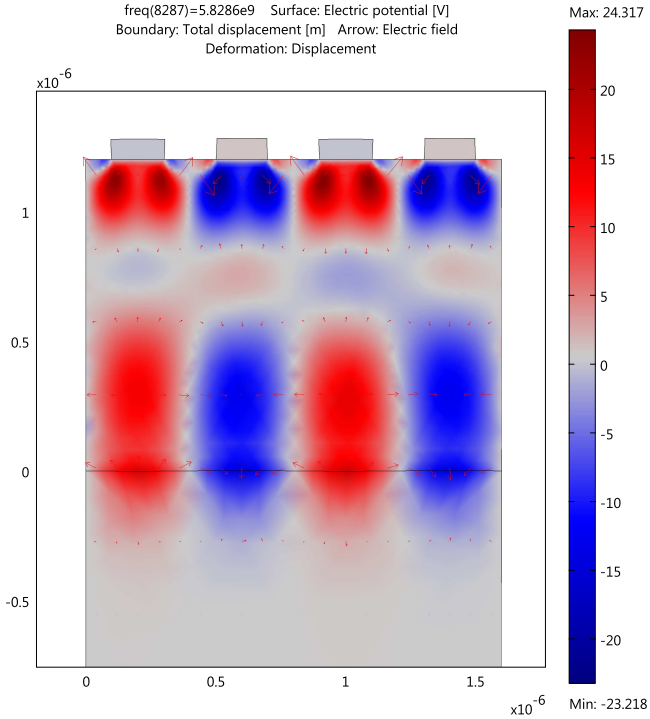


Fig 4.14. Electric potential of a SAW device of 200 nm IDT width, with resonance at 5.8286 GHz.

## 4.11. DIFFERENT SAW TOPOLOGIES

Three different models have been studied, where the IDT voltage is applied with different periodicity. The first model is the “Single-electrode” model where the IDTs have a periodic cell of a couple of IDTs, the first at 1 volt and the second one grounded. The wavelength is defined from the closest IDTs with the same voltage. So for finger width $p$ =200 nm as shown in Fig 4.1, the wavelength is $\lambda$=800 nm. The second model is the “Split-finger” where there are four IDTs in the cell, the first two with a voltage of one volt each and the next couple grounded. The total wavelength is the length of the four $p$ =200 nm IDTs and the distance between them, that is $\lambda$=1.6 μm, having a resonant frequency near 2.8 GHz. The third model is the “DART”, of which the modeled cell has one IDT in 1 Volt and the rest tree are grounded. Compared to the other models it can have more wavelengths of $\lambda_1$=800 nm and $\lambda_2$=1.6 μm at near 5.5 GHz and 2.1 GHz respectively.

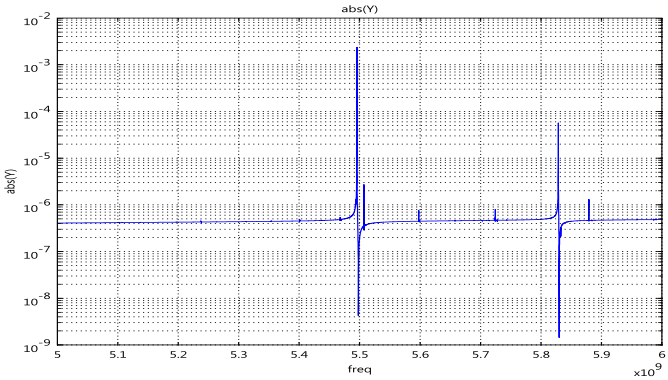


Fig 4.15 Admittance versus frequency for Single-electrode IDT with finger width 200 nm.

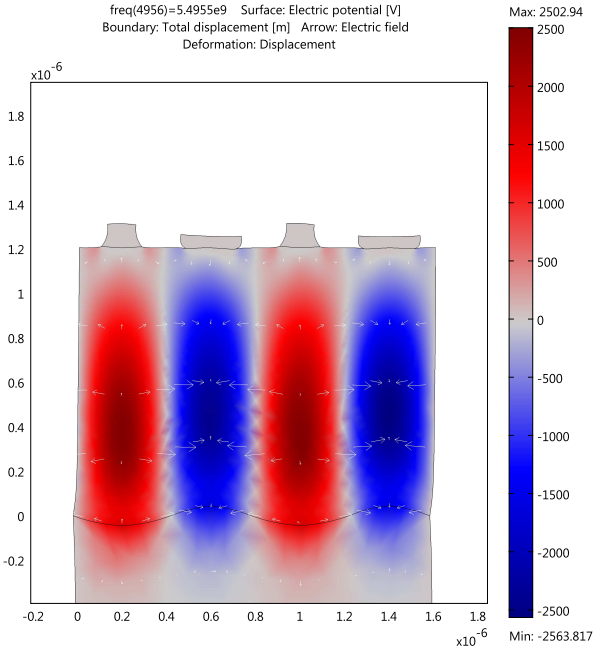


Fig 4.16. Single-electrode IDT of 200 nm width and 800 nm wavelength resonating at 5.4955 GHz

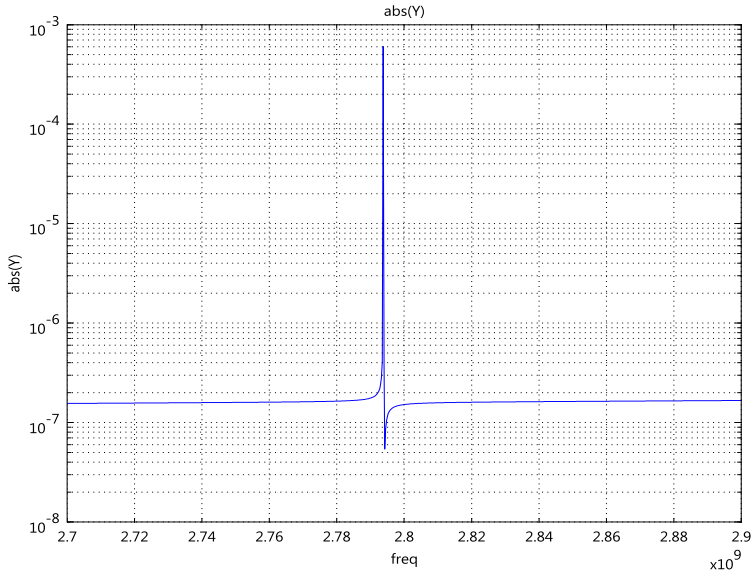


Fig 4.17. Admittance versus frequency for Split-electrode IDT with finger width 200 nm.

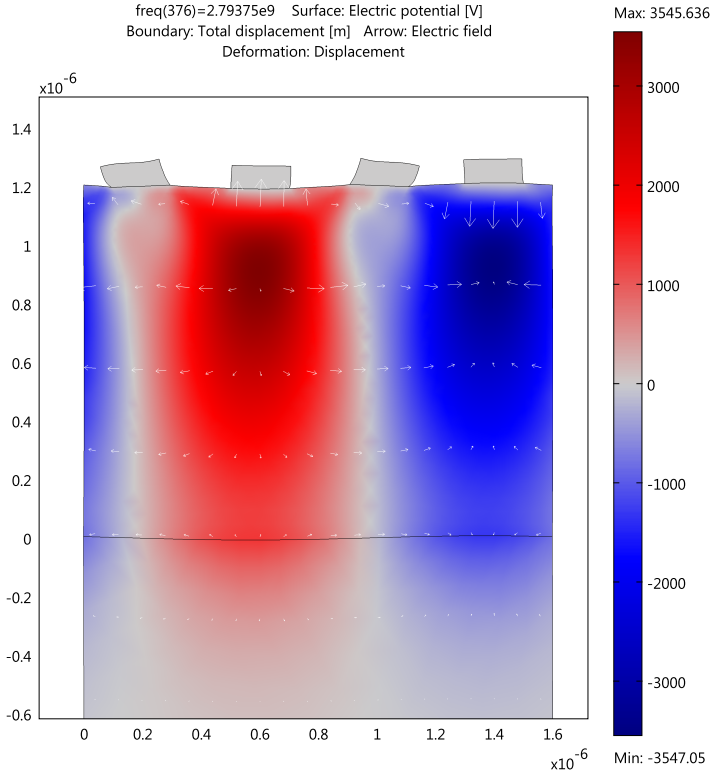


Fig 4.18. Split-Finger IDT of 200 nm width and 1.6 μm wavelength resonating at 2.7937 GHz

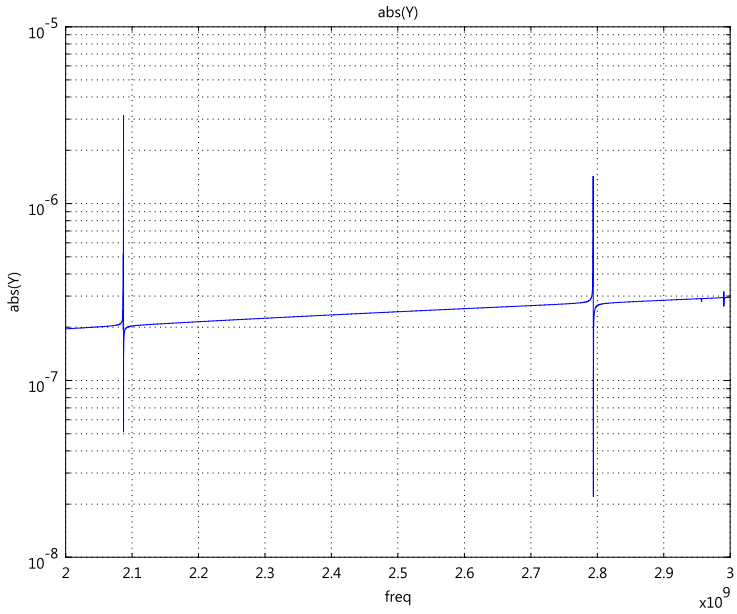


Fig 4.19. Admittance versus frequency for DART IDT structure with finger width 200 nm.

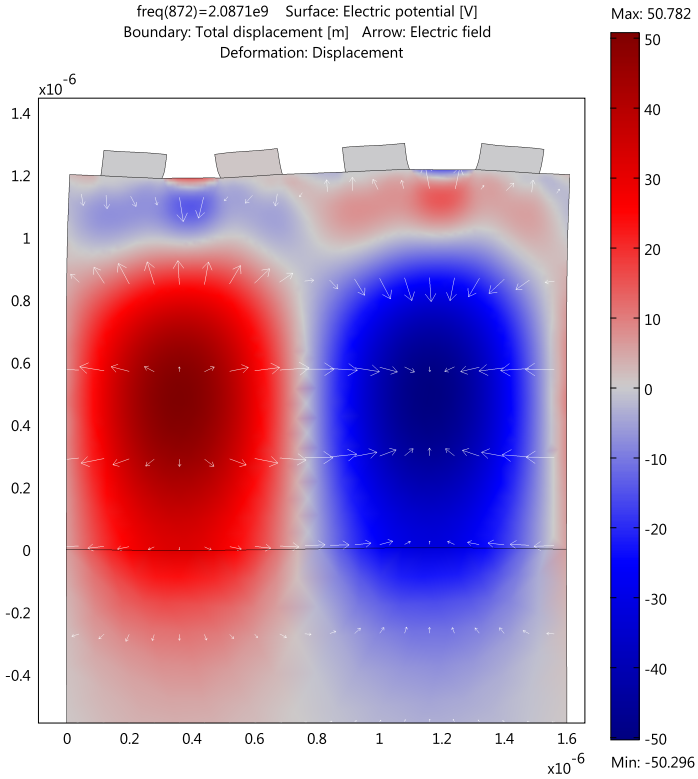


Fig 4.20 DART IDT of 200 nm finger width and 1.6 μm wavelength resonating at 2.0871 GHz

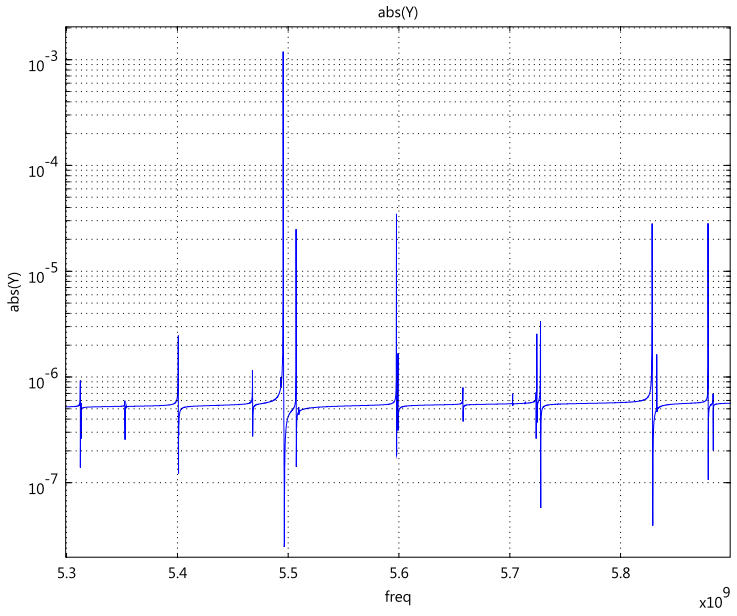


Fig 4.21. Admittance versus frequency for DART IDT structure with finger width 200 nm.

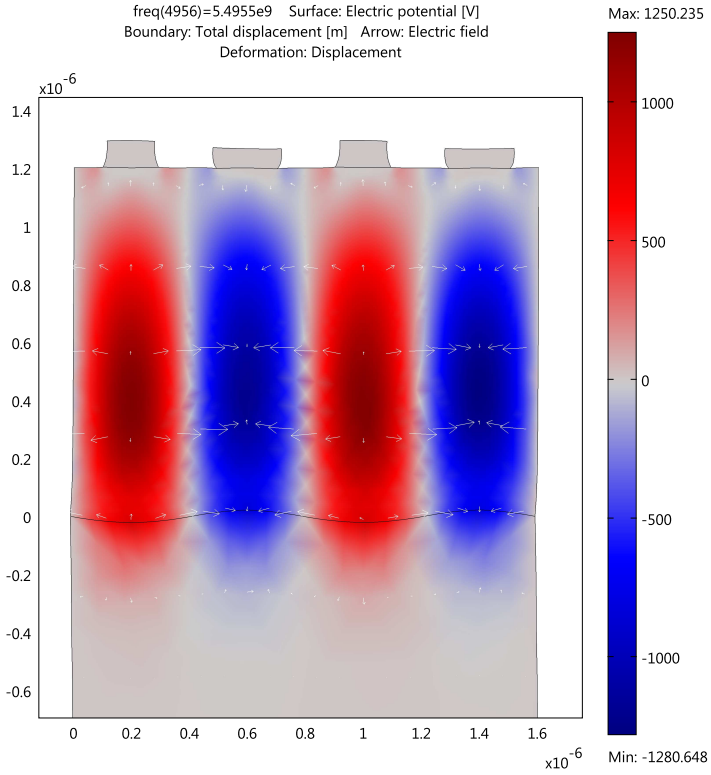


Fig 4.22. DART IDT structure of 200 nm finger width and 800 nm wavelength resonating at 5.4955 GHz

From the above simulations we have acquired the resonant frequencies for different IDT structures and investigated other physical properties, like electric potential and field, which occur during resonance. The values obtained are shown in the previous figures and they are going to be compared with experimental values obtained in the “Characterization” chapter.

An interesting result from these simulations is the distribution and mostly the intensity of the electric potential in the piezoelectric layer under the IDTs. Due to resonance, an amplified interference exist that forces the piezoelectric to oscillate at higher amplitudes than it normally would do with 1 volt on the IDTs. This is a vice versa property of the piezoelectric material that the electric potential defines the amplitude of the oscillation and reverse. So when the piezoelectric is forced to oscillate at these amplitudes it responds with very high electric potential that reaches three or more orders of the initial. In this measurement the resulted electric potential reached 3545 Volts (Fig 4.18) with an input of 1 Volt on the IDT array and can result in even higher values if a finer frequency step is used.

It is observed that the DART model has more resonant frequencies and this can be explained because three grounded IDT fingers exist for each IDT finger under 1V potential. Assuming that the peak of the acoustic wave should be positioned above the 1 volt IDT there are many wavelengths that correspond to this rule and more resonant frequencies can be created.

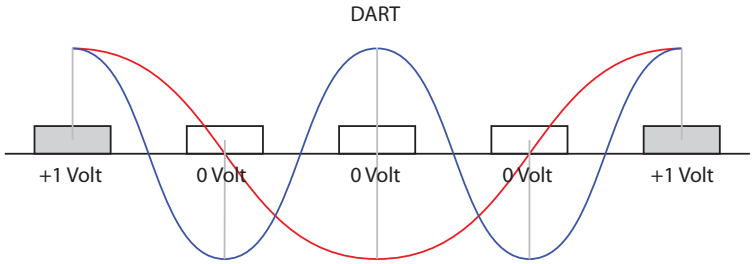


Fig 4.23. DART IDT array with multiple wavelengths on the same dimensions.

# FABRICATION

The substrate material used is the most common in semiconductors, that is Silicon (Si) because it easy to produce and has low cost. Silicon has a diamond cubic structure with a lattice spacing of 5.430710 Å (0.5430710 nm) while single crystal's structural and electronic properties are highly anisotropic.

Gallium nitride (GaN) is a binary III/V direct bandgap semiconductor which has a Wurtzite crystal structure. It is a highly polar and wide bandgap of 3.4 eV semiconductor. In contrast to former piezoceramics, GaN is a semiconducting piezomaterial and combines the piezoresistive and piezo-electric behaviors. Therefore, electromechanical investigations result in a so-called piezoresponse. With its large spontaneous polarization, several effects can contribute to the piezoresponse[4].
The growth of GaN on Si starts with a so-called seed layer which accommodates most of the lattice mismatch and helps in orienting the GaN grown on top of it. For a good GaN crystal orientation of the crystallites means not only the orientation along the c-axis, the preferred direction of growth (deviations are termed as tilt) but also the a-axis orientation of the crystallites parallel to each other (twist) Fig 5.1. When GaN is grown on Si, direction Si(111) is preferred which has a hexagonal arrangement of the Si atoms at the surface with a ~17% mismatch in atom positions Fig 5.2. Despite the large lattice mismatch the hexagonal arrangement of the Si atoms is helpful to orientate the seed layer so that the c-axis is oriented vertically to the substrate plane and the a-axis of the crystallites all parallel in-plane[6].

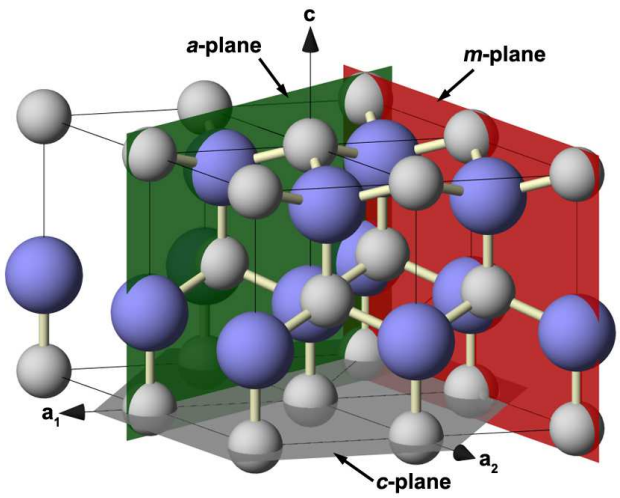


Fig 5.1. GaN molecular crystal structure[17]

GaN/Si wafers grown by MOCVD on high-resistivity (111)-oriented silicon wafers have been used. A buffer layer with a total thickness of 0.2 μm was grown between the silicon wafer and the 1-μm-thin undoped GaN top layer. The buffer layer, composed by AlN and $Al_xGa_{1-x}N$ layers (the thickness and the exact composition of each layer are not specified by the commercial provider), ensures a crack-free GaN top layer. The first step in the SAW structure manufacturing was the patterning and deposition of the connection pads.

For this, conventional photolithography, e-gun metallization (Ti/Au 20 nm/400 nm), and a liftoff technique have been used. A direct electron beam lithography writing, employing PMMA resist with a thickness of 200 nm, was developed for the IDT structure. The finger/interdigit dimension was 200 nm which corresponds to λ/2 = 400 nm for the acoustic wave. Finally, a Ti/Au (5 nm/75 nm) layer was selectively deposited by e-gun evaporation and a liftoff process.

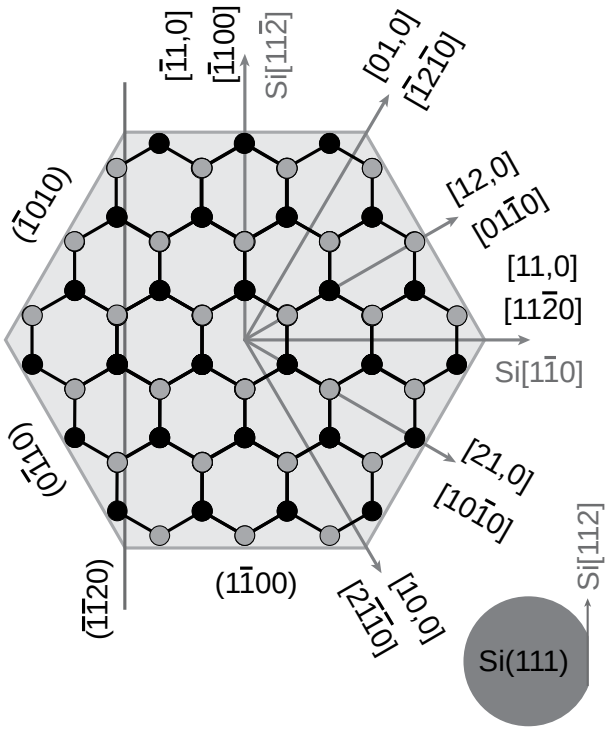


Fig 5.2. Epitaxial relationship of GaN(0001) on Si(111) which is GaN[11$\bar{2}$0]||Si[0$\bar{1}$1].[16]

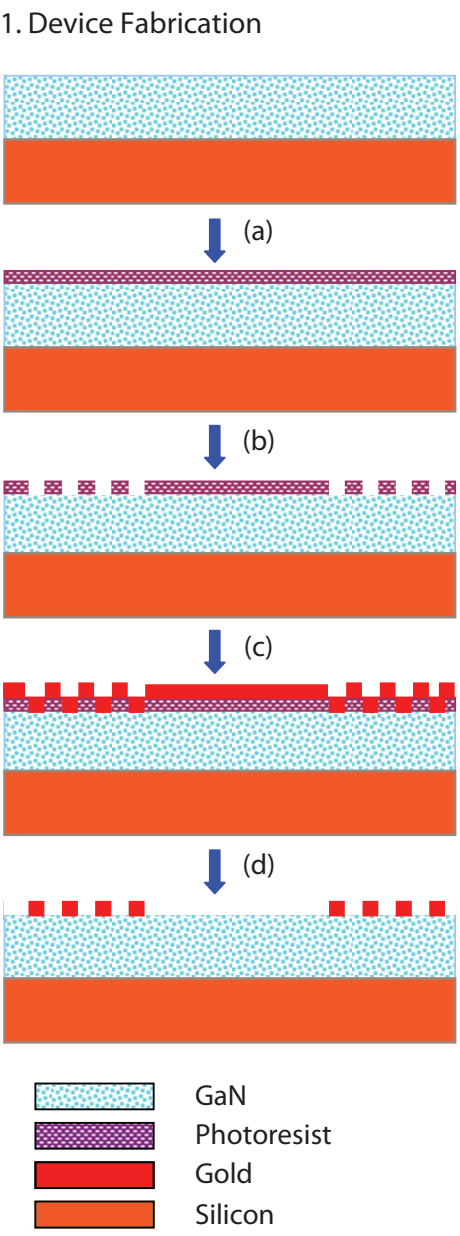


(a) A thin layer photoresist was spin-coated on a Gallium Nitride wafer,

(b) patterned using a UV light source and developed in photoresist developer.

(c) A metal layer of Gold (Au) was subsequently deposited on wafer using an e-beam evaporator,

(d) Followed by a lift-off procedure to form the interdigitated electrodes(IDTs) .

(e) Materials used for fabrication

Fig. 5.3. (a)-(d) shows the fabrication of SAW substrate. Cross-section of the device.

The basic fabrication steps are stated in Fig 5.4 and a more detailed description can be found at the references [1].

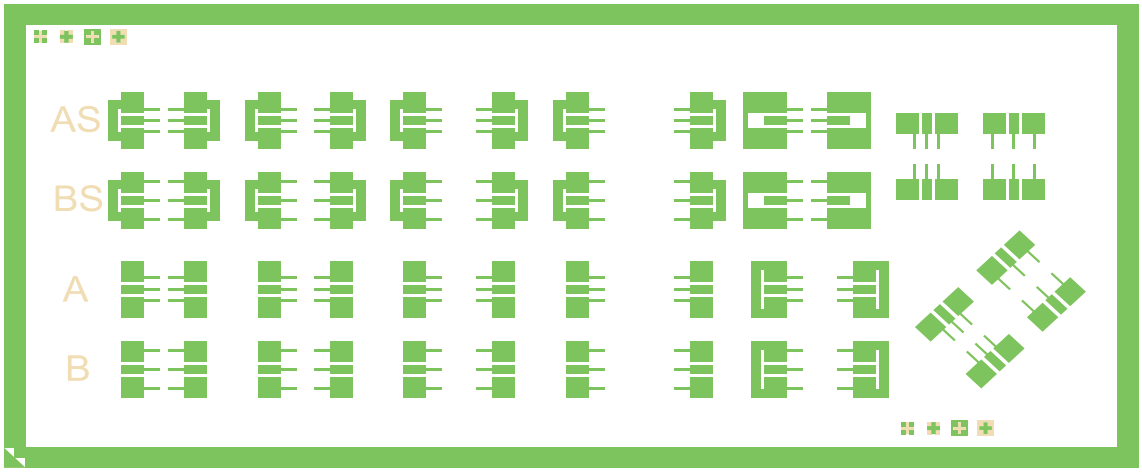


Fig 5.4. Design of a lithography mask of the pads without IDT structures.

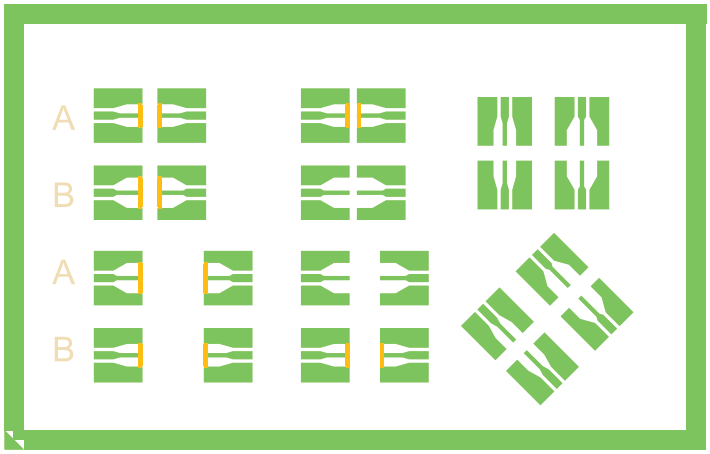


Fig 5.4. Masks design for SAW structures. Structures A are classic type and Structures B are DART/SPLIT finger

On the above photolithography masks that were used, it can be observed that many different structures have been designed, with variable delay lines, IDT lengths, crystalic orientation that the wave propagates on the material and reflectors been present or absent. All these parameters are changing the performance of the device and the characteristic resonating frequency. Below is shown a single delay line and its IDTs with extra magnification, in order to indicate the DART type structure.

Fig 5.6. Design of the fabrication mask. A single delay line left. Magnification of IDT fingers right.

Post fabrication photos from Scanning Electron Microscope (SEM).

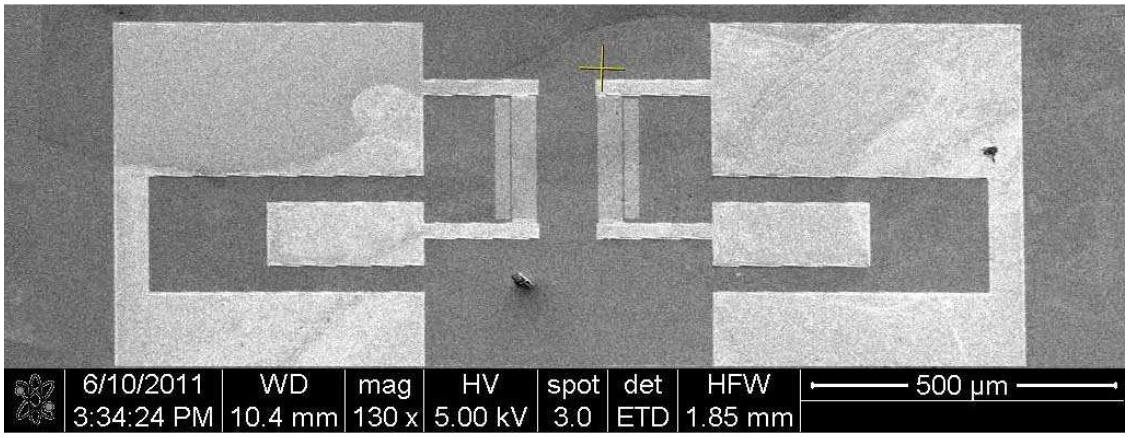


Fig. 5.7a Complete IDT structure with connecting pads at magnification x130

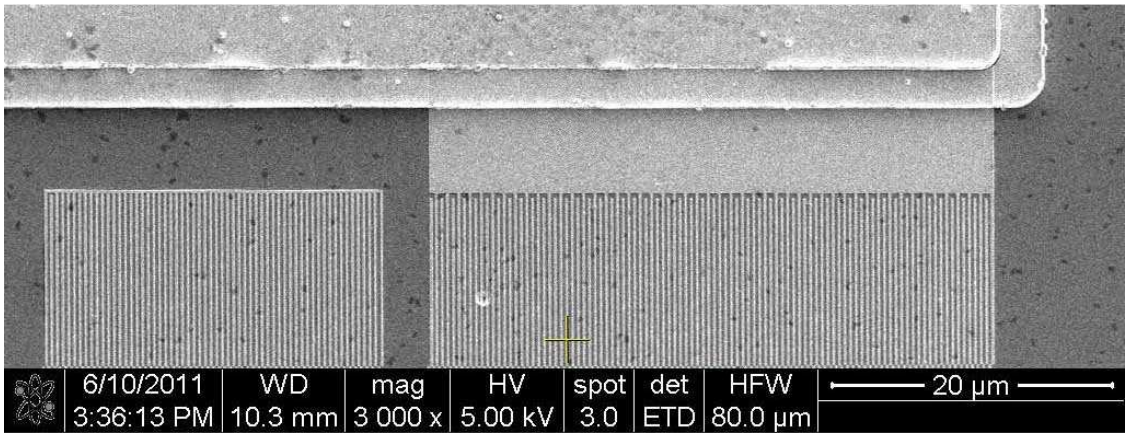


Fig. 5.7b IDT fingers with reflectors at magnification x3000

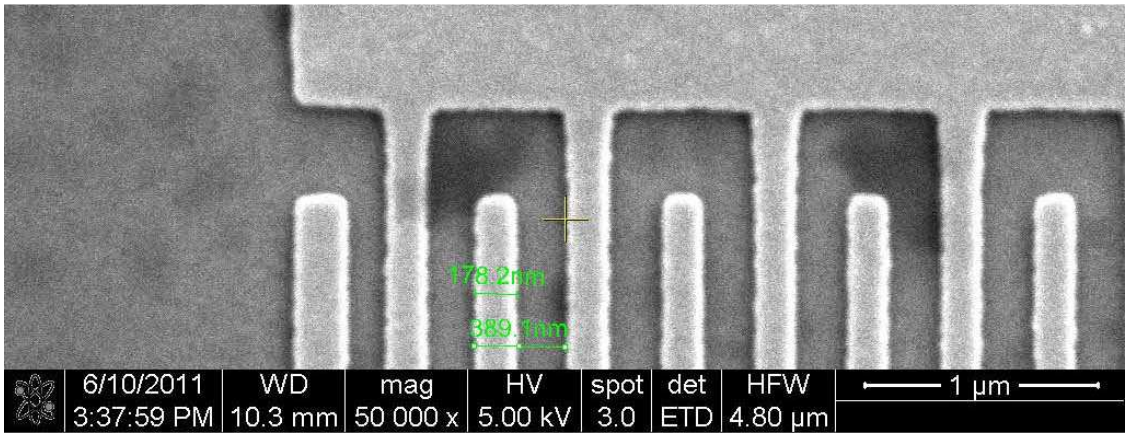


Fig. 5.7c Single electrode IDT type, magnification x50000

Types of the fabricated IDT arrays under the SEM, with 130/200/200nm finger width respectively for the following images.

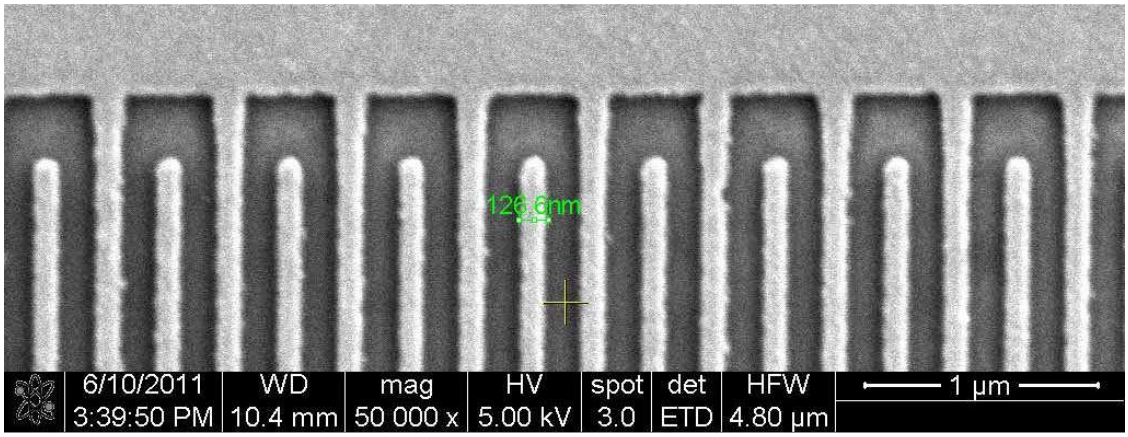


Fig. 5.8a Single electrode type IDT array, finger width 130nm and metallization ratio η=0.5.

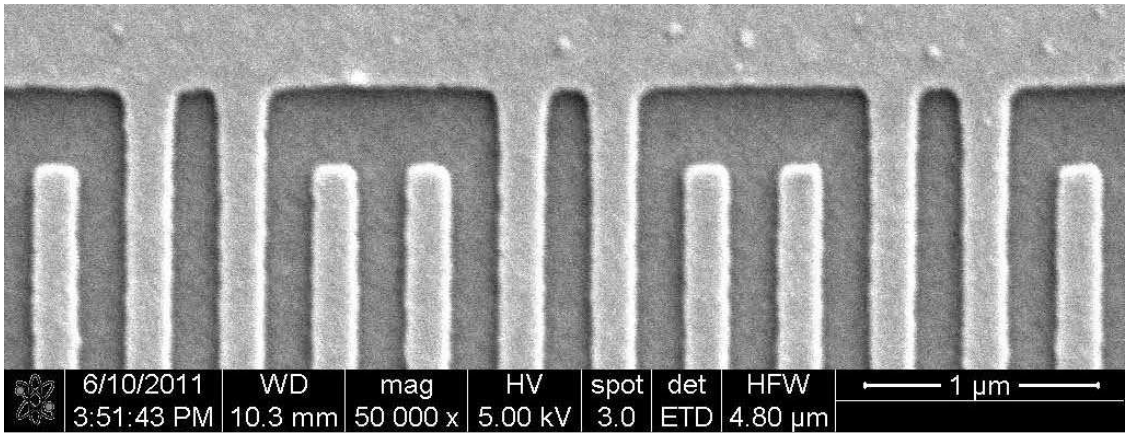


Fig. 5.8b Split electrode type IDT array, finger width 200nm and metallization ratio η=0.5.

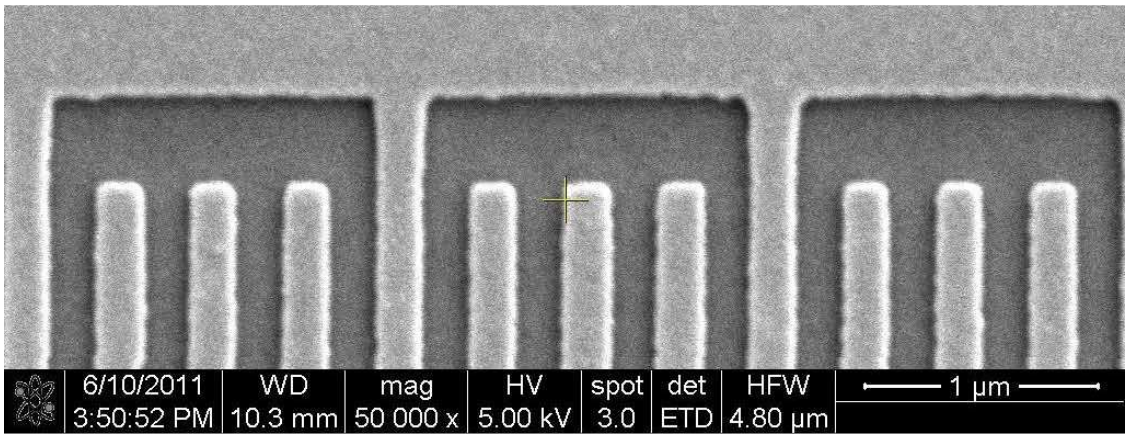


Fig. 5.8c DART type IDT array, finger width 200nm and metallization ratio η=0.5.

# CHARACTERIZATION

After the fabrication process completed the structures were measured. As seen in Fig 6.1 a couple of three-finger probes were placed on the large conducting area of the IDTs. The middle golden area a grounded probe was put, and the upper and lower golden areas two probes have been placed, with the same alternating current with potential of 1 Volt. The scanned frequency of the alternating current was from 2, till 9 GHz depending the IDT type. .

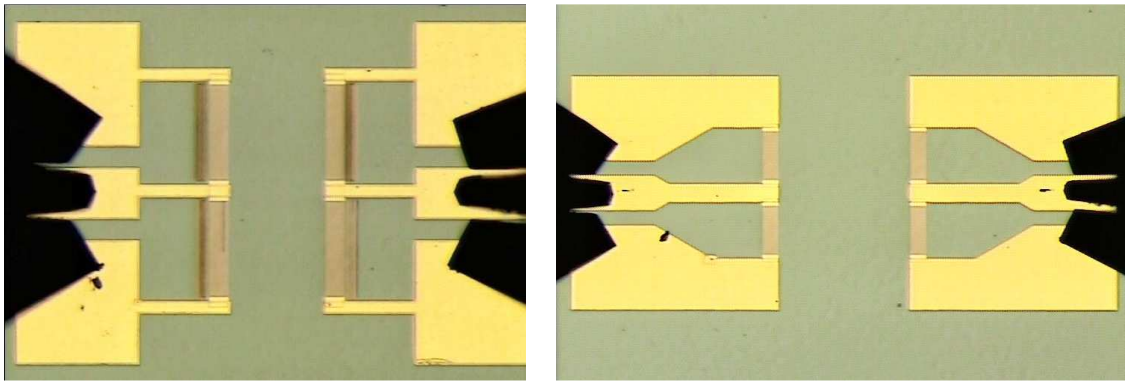

Fig 6.1 Photograph from optical microscope of two delay lines. On the left image, reflectors exist but not on the right. The type of the IDT array in this image cannot be defined due to the lack of discreteness of the fingers.

For the characterization scattering parameters (S-parameters) were measured and then compared with the simulated results.

S-parameters describe the response of an N-port network to voltage signals at each port. The first number in the subscript refers to the responding port, while the second number refers to the incident port. Thus S21 means the response at port 2 due to a signal at port 1.

For a two-port network, the incident voltage at each port is denoted by "a", while the voltage leaving a port is denoted by "b". We assume that the two voltages are traveling in opposite directions so they can occur at the same node.

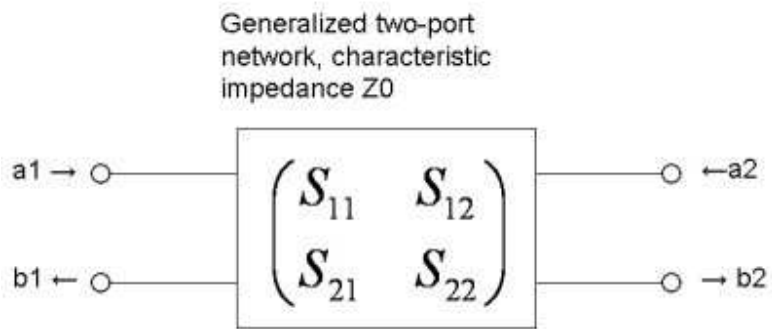

If we assume that each port is terminated in impedance Z0, we can define the four S-parameters of the 2-port as:

$$S_{11} = b1/a1$$
$$S_{12} = b1/a2$$
$$S_{21} = b2/a1$$
$$S_{22} = b2/a2$$

For port n, the associated S-parameter definition is in terms of incident and reflected 'power waves', and respectively [39]

$$a = \frac{1}{2}k(V + Z_p I) \qquad b = \frac{1}{2}k(V - Z_p^* I)$$

Here's the matrix algebraic representation of 2-port S-parameters:

$$\begin{pmatrix} b_1 \\ b_2 \end{pmatrix} = \begin{pmatrix} S_{11} & S_{12} \\ S_{21} & S_{22} \end{pmatrix} \times \begin{pmatrix} a_1 \\ a_2 \end{pmatrix}$$

If we want to measure S11, we inject a signal at port one and measure its reflected signal. In this case, no signal is injected into port 2, so a2=0; during all laboratory S-parameter measurements, we only inject one signal at a time. If we want to measure S21, we inject a signal at port 1, and measure the resulting signal exiting port 2. For S12 we inject a signal into port 2, and measure the signal leaving port 1, and for S22 we inject a signal at port 2 and measure its reflected signal. All of the a and b measurements are vectors. [22]
S-parameter magnitudes are presented in one of two ways, linear magnitude or decibels (dB). Because S-parameters are a voltage ratio, the formula for decibels in this case is

$$S_{ij}(dB) = 20*\log[S_{ij}(magnitude)]$$

Admittance (Y) is a measure of how easily a circuit or device will allow a current to flow. It is defined as the inverse of the impedance (Z). The SI unit of admittance is the siemens.

$$Y = Z^{-1} = 1/Z$$

In the following figures are presented S-parameters for the frequency range that resonance was observed. Below is compared with the simulated admittance (Y-parameters) for in the same frequency spectrum. The measurements where performed on Single-electrode, Split-electrode and DART IDT type devices with 200 nm and 130 nm finger width.

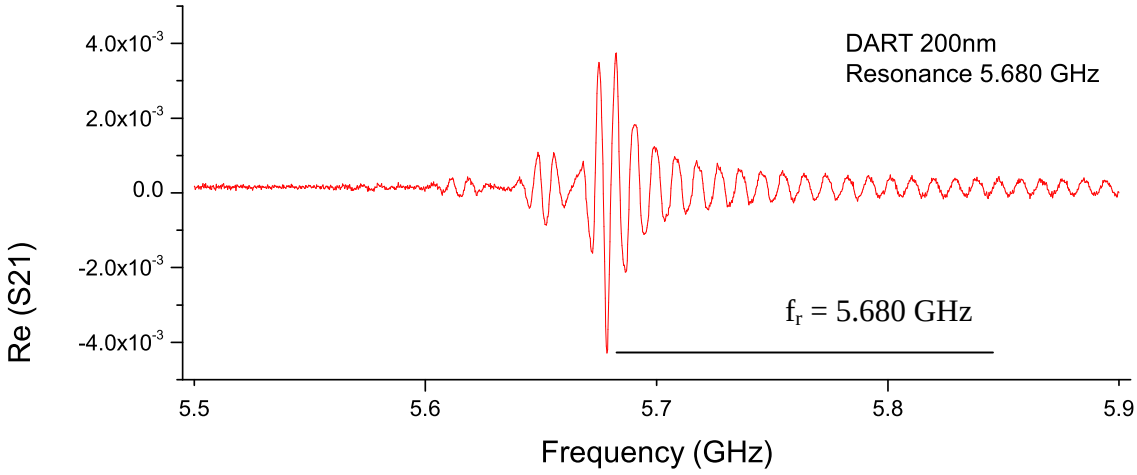


Fig 6.2 Measured S-parameters versus frequency of SAW DART IDT structure 200 nm finger width

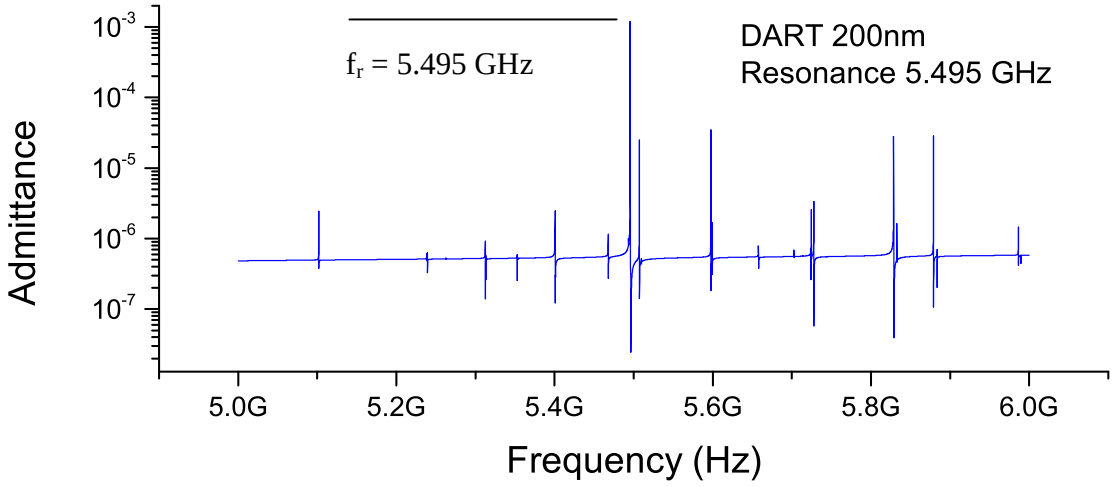


Fig 6.3 Admittance versus frequency retracted from Comsol simulation.

The simulations for the DART electrodes with 200nm width had a frequency drift of 185 MHz to lower frequencies that is 3.25% difference from the characterized device. The simulated resonant frequency was relatively very close to the measured frequency

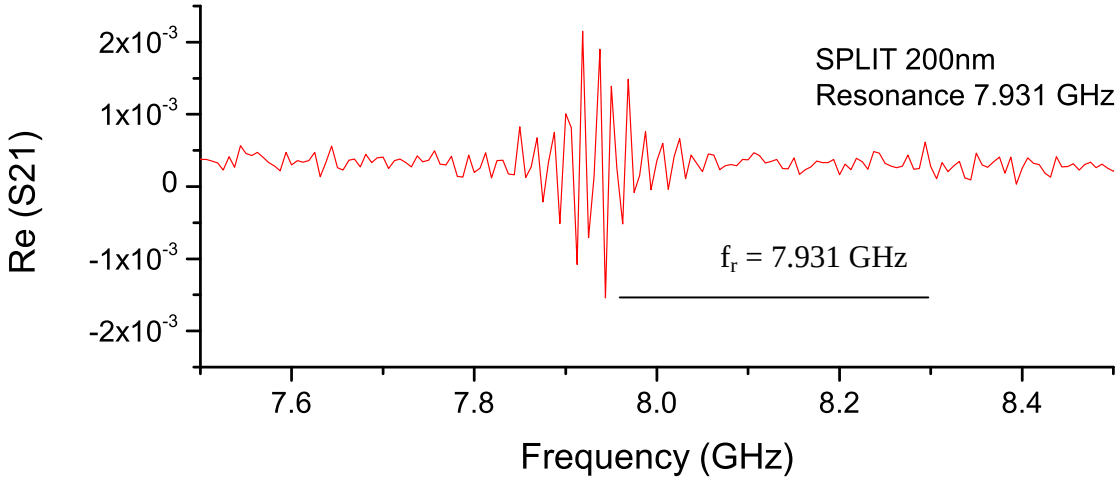


Fig 6.4 Measured S-parameters versus frequency of SAW Split-electrode IDT structure with 200 nm finger width.

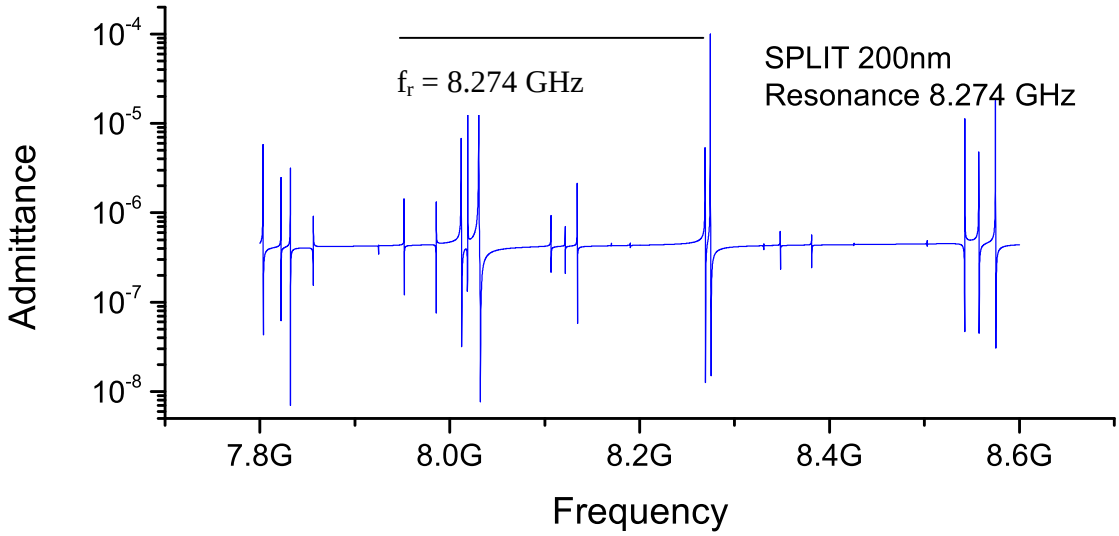


Fig 6.5 Admittance versus frequency retracted from Comsol simulation.

The simulations for the Split-electrodes with 200nm finger width had a frequency drift of 343 MHz to higher frequencies that is 4.14% difference from the characterized device.

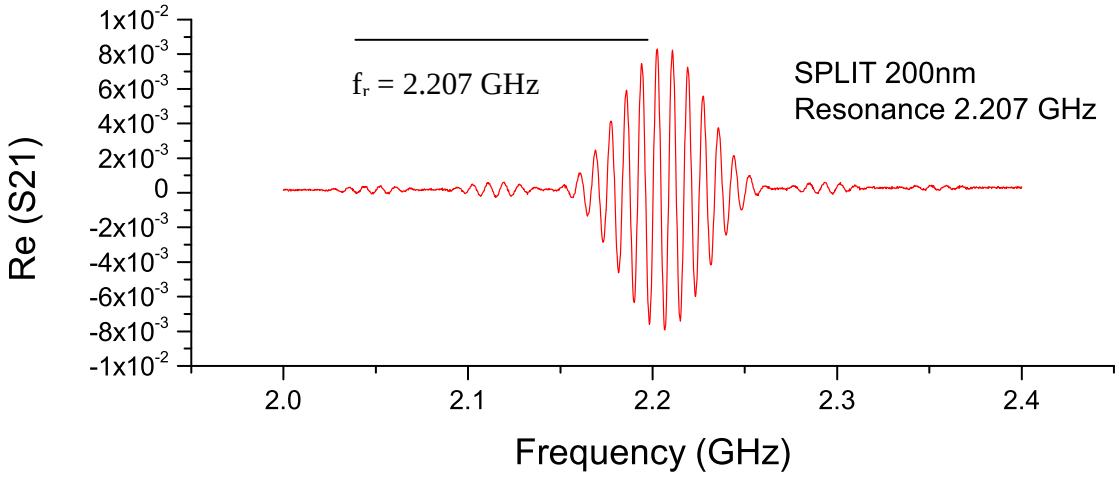


Fig 6.6 Measured S-parameters versus frequency of SAW Split-electrode IDT structure with 200 nm finger width at a harmonic resonant frequency.

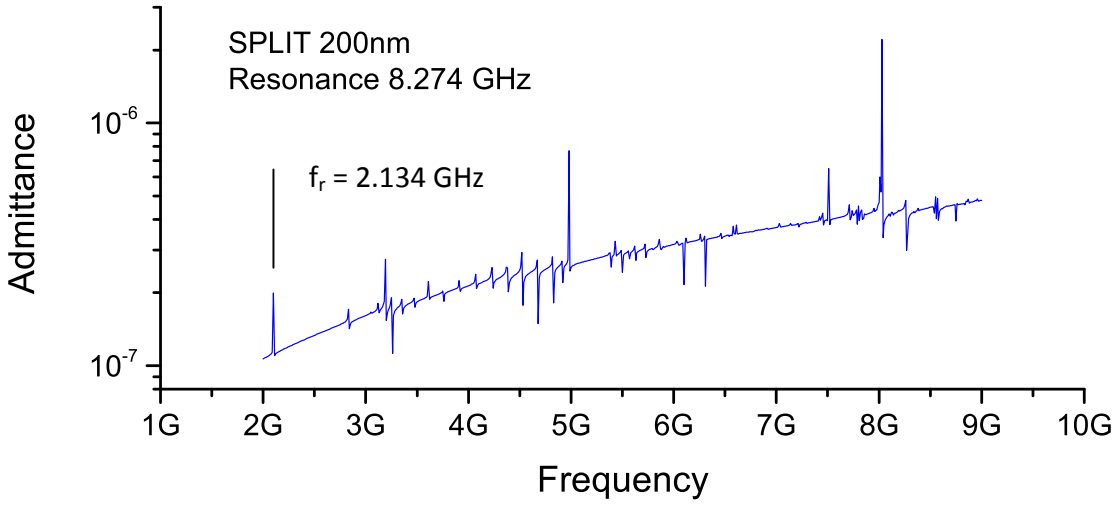


Fig 6.7 Admittance versus frequency retracted from Comsol simulation for a wider frequency spectrum.

The simulations of the Split-electrodes with 200nm width for a wider frequency spectrum had a harmonic resonance drift of 73 MHz to lower frequencies that is 3.42% difference from the characterized device. The main resonant frequency was compared in the previous figure.

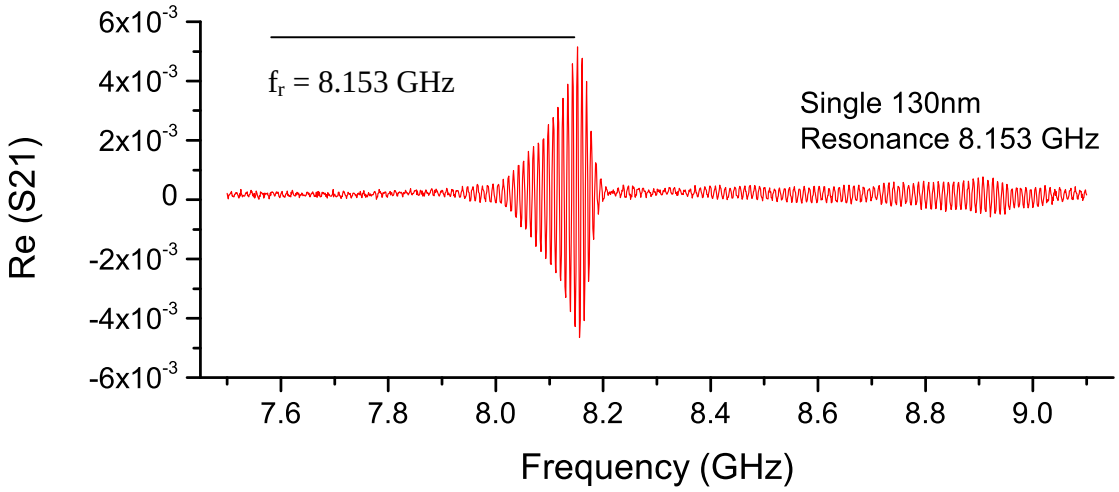


Fig 6.8 Measured S-parameters versus frequency of SAW Single-electrode IDT structure with 130 nm finger width.

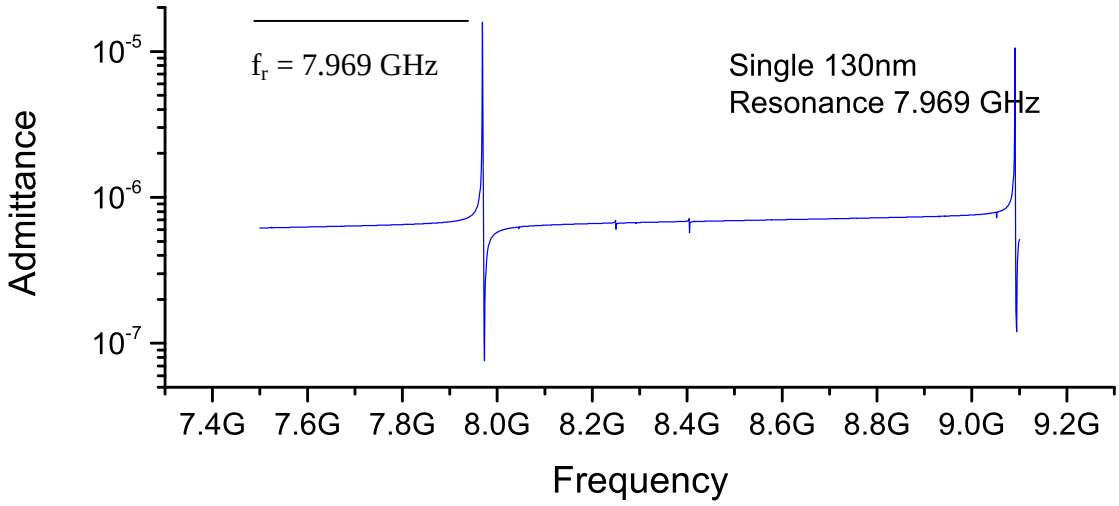


Fig 6.9 Admittance versus frequency retracted from Comsol simulation.

The simulations for the Single-electrodes with 130nm width had a frequency drift of 184 MHz to lower frequencies that is 2.25% difference from the characterized device.

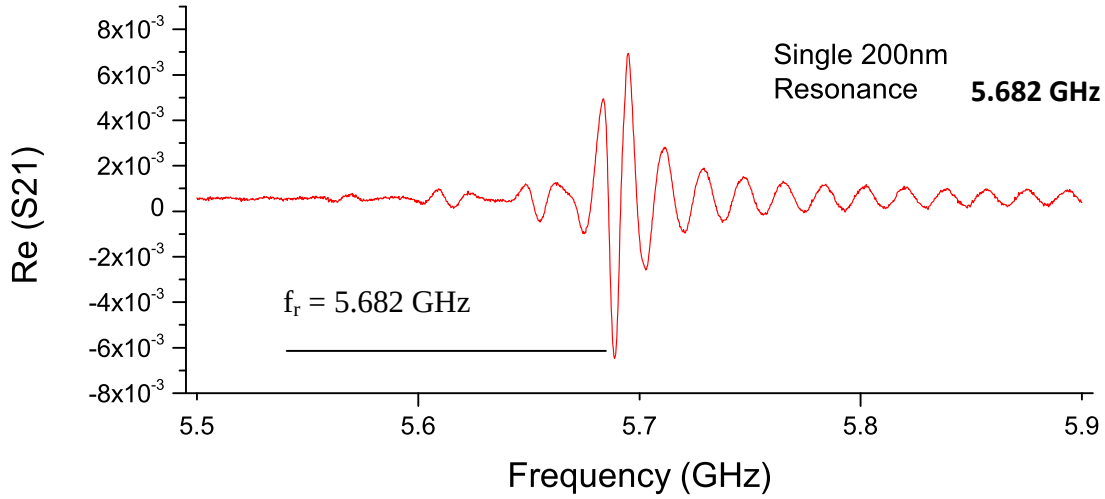


Fig 6.10 Measured S-parameters versus frequency of SAW Single-electrode IDT structure with 200 nm finger width.

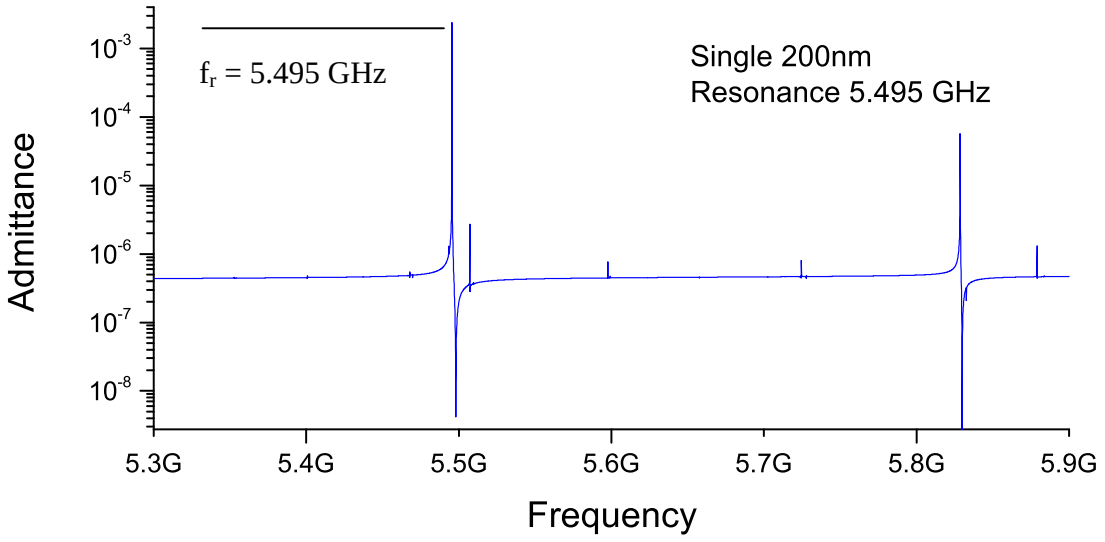


Fig 6.11 Admittance versus frequency retracted from Comsol simulation.

The simulations for the Single-electrodes with 200nm width had a frequency drift of 187 MHz to lower frequencies that is 3.29% difference from the characterized device.

# CONCLUSIONS

A finite element model has been developed using COMSOL Multiphysics. The results that have been obtained using FEM present less than 5% difference from the experimental results that are considered reasonably accurate. The only parameters that were needed to be introduced to the FE simulation was material properties and model dimensions. The prediction of the exact admittance has not been possible due to the application of infinite boundary condition (non-finite periodicity) and non-inclution of various attenuation effects. The limitation of this simulator is mainly due to the constraint on the computing resources but not due to the FE method itself.

Substrate and piezoelectric layer height are changing the admittance of the device, while electrode height (electrode mass) is changing the center resonant frequency. The lack of the third dimension in our model was justified by the increased size of the problem incapable of being solved due to the extent amount of equations. The size of the device was set to ten times the wavelength for the substrate height and the number of the elements was optimized for acceptable accuracy in frequency response compromising in calculation performance.

To determine the parameters which affect the bandwidth and center frequencies a series of simulations were done for various IDT structure types like Single-electrode, Split-electrode and DART. For two different finger widths the simulated results compared with the experimental presented differences of less than 5% in center resonance frequency of all the tested devices. SAW devices (GaN/Si) designed and implemented with fs up to 9GHz.

# Apendix - Constants used in Comsol parameters

**GaN** constants table

Elasticity Matrix

$C_E$ =

| | | | | | |
|---|---|---|---|---|---|
| $3{,}9\times10^{11}$ | $1{,}45\times10^{11}$ | $1{,}06\times10^{11}$ | 0 | 0 | 0 |
| $1{,}45\times10^{11}$ | $3{,}9\times10^{11}$ | $1{,}06\times10^{11}$ | 0 | 0 | 0 |
| $1{,}06\times10^{11}$ | $1{,}06\times10^{11}$ | $3{,}98\times10^{11}$ | 0 | 0 | 0 |
| 0 | 0 | 0 | $1{,}05\times10^{11}$ | 0 | 0 |
| 0 | 0 | 0 | 0 | $1{,}05\times10^{11}$ | 0 |
| 0 | 0 | 0 | 0 | 0 | $1{,}225\times10^{11}$ |

Sub.2 GaN – Piezo, xz plane,

$C_E$ =

| | | | | | |
|---|---|---|---|---|---|
| 0 | 0 | 0 | 0 | -0,3 | 0 |
| 0 | 0 | 0 | -0,3 | 0 | 0 |
| -0,36 | -0,36 | 1 | 0 | 0 | 0 |

Coupling matrix, stress-change form

e =

| | | | | | |
|---|---|---|---|---|---|
| 0 | 0 | 0 | 0 | -0.3[C/m$^2$] | 0 |
| 0 | 0 | 0 | -0.3[C/m$^2$] | 0 | 0 |
| -0.34[C/m$^2$] | -0.34[C/m$^2$] | 0.67[C/m$^2$] | 0 | 0 | 0 |

Density ρ = 6150 Kg/m$^3$

Relative permittivity $E\tau = 9$

## **Au** constants table

Heat capacity at constant pressure C = 129[J/(kg*K)]

Youngs modulus E = $7.9\times10^{10}$ [Pa]

Thermal expansion coefficient α = 14.2e-6[1/K]

Thermal conductivity k = 317[W/(m*K)]

Poisson's ratio $\nu$ = 0.44

Density ρ = 19300[kg/m$^3$]

Electric conductivity σ = 45.6e6[S/m]

# REFERENCES

[1] Alexandru Müller, Member, IEEE, Dan Neculoiu, Member, IEEE, George Konstantinidis, George Deligeorgis,Adrian Dinescu, Antonis Stavrinidis, Alina Cismaru, Mircea Dragoman, Alexandra Stefanescu "SAW Devices Manufactured on GaN/Si for Frequencies Beyond 5 GHz". 2010 IEEE

[2] Stefanescu, A. Muller, A. Dinescu, G. Konstantinidis, A. Cismaru,A. Stavrinidis, D. Neculoiu "FEM ANALYSIS OF GaN BASED SURFACE ACOUSTIC WAVE RESONATORS". ISBN 978-1-61284-173-1

[3] Lifeng Qin and Qing-Ming Wang[a] (2010) "Analysis of dual-mode thin film bulk acoustic resonators based on polar *c*-axis tilted wurtzite gallium nitride"

[4] S. Trolier-McKinstry (2008). "Chapter3: Crystal Chemistry of Piezoelectric Materials". In A. Safari, E.K. Akdo˘gan. *Piezoelectric and Acoustic Materials for Transducer Applications*. New York: Springer. ISBN 9780387765389.

[5] Alexander S. Rukhlenko "Charge Distribution and Capacitance Calculation for Generalized Periodic SAW Transducers Using Floquet's Technique". Dept. of Semiconductor Physics, Belarusian State University

[6] Bougrov V., Levinshtein M.E., Rumyantsev S.L., Zubrilov A., in *Properties of Advanced Semiconductor Materials GaN, AlN, InN, BN, SiC, SiGe*. Eds. Levinshtein M.E., Rumyantsev S.L., Shur M.S., John Wiley & Sons, Inc., New York, 2001, 1–30

[7] H. Amano et al. (1986). "Metalorganic vapor phase epitaxial growth of a high quality GaN film using an AlN buffer layer". Applied Physics Letters

[8] T. Zimmermann, M. Neuburger, P. Benkart, F. J. Hernández-Guillén, C. Pietzka, M. Kunze,I. Daumiller, A. Dadgar, A. Krost, and E. Kohn "Piezoelectric GaN Sensor Structures", May 2006

[9] A.R.Baghai-Wadji, S . Selberherr, and F. Sei fert . 'On the calculation of charge, electrostatic potential and capacitance in generalized finite SAW structure, " in IEEE Ultrason. Symp. Proc., 1984, pp. 44-48.

[10] D.P.Morgan. Surface-wave devices for signal processing, Elsevier, Amsterdam, 1985, ch.4.

[11] B.Lewis, P.M.Jordan, R.F.Milsom, and D.P.Morgan. "Charge and field superposition methods for analysis of generalized SAW interdigital transducers," in IEEE Ultrason. Symp. Proc., 1979, pp. 709-714

[12] R.C.Peach. "A general approach to the electrostatic problem of the SAW interdigital transducers," IEEE Trans. Son. Ultrason., vol. SU-28, pp. 96-105, March 1981.

[13] H.Engan. "Surface acoustic wave multielectrode transducers," IEEE Trans. Son. Ultrason., vol. SU22, pp. 395-401, NOV. 1975

[14] Ken-Ya Hashimoto "Surface Acoustic Wave Devices in Telecommunications: Modelling and Simulation" ISBN 978-3540672326 Springer 2000

[15] David Morgan “Surface Acoustic Wave Filters, Second Edition: With Applications to Electronic Communications and Signal Processing (Studies in Electrical and Electronic Engineering)” by ISBN 978-0123725370

[16] Alois Krost, Armin Dadgar “GaN-based optoelectronics on silicon substrates”

[17] Paskova, Tanya (Hrsg.) “Nitrides with Nonpolar Surfaces Growth, Properties, and Devices” ISBN 978-3-527-40768-2 - Wiley-VCH, Berlin

[18] Sophocles J. Orfanidis "Electromagnetic Waves and Antennas" 2008

[19] J Choma & WK Chen (2007). Feedback networks: theory and circuit applications. Singapore: World Scientific. Chapter 3, p. 225 ff. ISBN 981-02-2770-1.

[20] R. Mavaddat. (1996). "Network scattering parameters". Singapore: World Scientific. ISBN 978-981-02-2305-2

[21] Kurokawa, K., "Power Waves and the Scattering Matrix", IEEE Trans. Micr. Theory & Tech.

[22] John Choma; W. K. Chen "Feedback Networks : Theory and Circuit Applications" ISBN 9810227701.

[23] C. S. Hartmann, P. V. Wricjht, R. J. Kansy, and E. M. Garber “AN ANALYSIS OF SAW INTERDIGITAL TRANSDUCERS WITH INTERNAL REFLECTIONS AND THE APPLICATION TO THE DESIGN OF SINGLE-PHASE UNIDIRECTIONAL TRANSDUCERS” RF Monolithics, Inc. Dallas, Texas

[24] P. V. Wright, and S. A. Wilkus “A PROTOTYPE LOW-LOSS FILTER EMPLOYING ;ZINGLE-PHASE UNIDIRECTIONAL TRANSDUCERS” RFMonolithics Inc. 4441 Sigma Road Dallas, Texas

[25] K. Yamanouchi and H. Furuyashiki “LOW-LOSS SAW FILTER USING INTERNAL REFLECTION TYPES OF NEW SINGLE-PHASE UNIDIRECTIONAL TRANSDUCER”

[26] Masao Takeuchi, Kazumhiko Yamanouchi “New Types of SAW Reflectors and Resonators Consisting of Reflecting Elements with Positive and Negative Reflection Coefficient”

[27] David P. Morgan “Reflective Array Method for Analysis and Design of Weighted DART Transducers and Filters”

[28] R. Dill*, W. Rude*, B. Lewis “The Splitfinger Directional Transducer (SFDT): A New Single Phase Unidirectional Transducer”

[29] Qiuyun Fu*, Helmut Stab, Wolf-Joachim Fischer “Investigation of Single-Finger Interdigital Transducer as Programmable Reflector”

[30] T. Kodama, H. Kawabata, Y. Yasuhara and H. Sat0 “DESIGN OF LOW-LOSS SAW FILTERS EMPLOYING DISTRIBUTED ACOUSTIC REFLECTION TRANSDUCERS”

[31] Peter M. Smith “Studies of Surface Acoustic Wave Interdigitated Transducers”

[32] Bill J. Hunsinger,Kentaro Hamma “Surface acoustic wave device with reflection suppression”.

[33] S. Trolier-McKinstry (2008). "Chapter3: Crystal Chemistry of Piezoelectric Materials". In A. Safari, E.K. Akdo˘gan. *Piezoelectric and Acoustic Materials for Transducer Applications*. New York: Springer. ISBN 9780387765389.

[34] R.F.Mitchell and D.W.Parker,”Synthesis of acoustic-surface-wave filters using double elecrodes” Electronics Letters, vol.10, p.512,1974.

[35] M.Takeuchi, K.Yamanouchi, K.Murata and K.Doi, “Floating-electrode-type SAW unidirectional transducers using leaky surface waves and their application to low-loss filters,” Electronics and Communications in Japan, Part3, vol. 76, pp. 99-110, 1993.

[36] W.R.Smith and W.F.Pedler,”Fundamental- and harmonic-frequency cirquit model analysis of interdigital transducers with arbitrary metallization ratios and polarity sequences,” IEEE Trans. Microwave Theory and Techniques, vol. MTT-23, pp. 853-864, Nov. 1975.

[37] S.Datta Surface Acoustic Wave Devices, Prentice-Hall, Englewood Cliffs, p. 178, 1986.

[38] J.M. Hodé, J. Desbois, P. Dufilié, M.Solal and P. Ventura. ‘SPUDT-based filters: design principles and optimisation’. Proc. IEEE Ultrason. Symp., 1995, pp. 39-50.

[39] Kurokawa, K., "Power Waves and the Scattering Matrix", IEEE Trans. Micr. Theory & Tech.